

---

# Chapter V

## Modification of Chitosan and CP Blend-based Biodegradable Polymer Nanocomposites by Irradiation with MeV Ions

---

- 5.1 INTRODUCTION
- 5.2 RESULTS AND DISCUSSION
  - 5.2.1 XRD Analysis
  - 5.2.2 ATR-FTIR Analysis
  - 5.2.3 Optical Analysis
  - 5.2.4 AC Electrical Frequency Response
  - 5.2.5 SEM Analysis
  - 5.2.6 AFM Analysis
- 5.3 CONCLUSIONS
- REFERENCES

---

Papers published in peer-reviewed journals related to this chapter:

1. Effect of swift heavy ions irradiation on physicochemical and dielectric properties of chitosan and chitosan-Ag nanocomposites  
**Gnansagar B. Patel**, N.L. Singh, F. Singh, P.K. Kulriya  
*Radiat. Phys. Chem.* 181 (2021) 109288.  
doi:[10.1016/j.radphyschem.2020.109288](https://doi.org/10.1016/j.radphyschem.2020.109288)
2. MeV ions induced modification in structural, optical, dielectric and surface morphological properties of (chitosan-PEO)-Ag nanocomposites  
**Gnansagar B. Patel**, N.L. Singh, F. Singh, P.K. Kulriya  
(Communicated)

# Chapter V

## Modification of Chitosan and CP Blend-based Biodegradable Polymer Nanocomposites by Irradiation with MeV Ions

### 5.1 Introduction

An augmenting requisite to cultivate environment-friendly materials with enhanced functionalities such as sophisticated mechanical, thermal and chemical stability with biodegradation feature encourages to elaboration of flexible nanocomposites system based on green polymers. These materials have distinctive signature perspectives such as ease of processability, low-weight, economical, energy and time conserving, fatigue and corrosion resistance, etc. [1]. These features explicitly relied on the characteristics of the host and kind of micro to nano-sized fillers. Moreover, the nano-sized filler of dimension less than 100 nm prevailing unique behavior owing to the quantum size effect as compare to bulk [2]. The nanoparticles used as reinforcing are of conducting nature capably yields the matrix of superior dielectric and conductivity properties, which can be used in contrives into fields where such soft and flexible semiconducting and conducting materials being potentially encouraged to use [3]. An enormous efforts are established by concerning the natural and biodegradable nanocomposites in distinctive areas dealing with sensors, photovoltaic cells, UV and electromagnetic shielding materials, actuators, microwave absorbers, robotics, and wearable medical devices, etc. [1,4]. In the present chapter, biodegradable polymer nanocomposites, namely, chitosan–Ag and CP blend–Ag nanocomposites systems to be pretended and functionalized using MeV ions. The important signatures and literature reviewed relevant to these matrices discussed in Chapter 1 (section 1.4.3). The preparation of self-standing matrices, MeV ions irradiation and subsequent characterizations were explained in sections 2.2, 2.3 and 2.3 of Chapter 2, respectively.

## 5.2 Results and Discussion

### 5.2.1 XRD Analysis

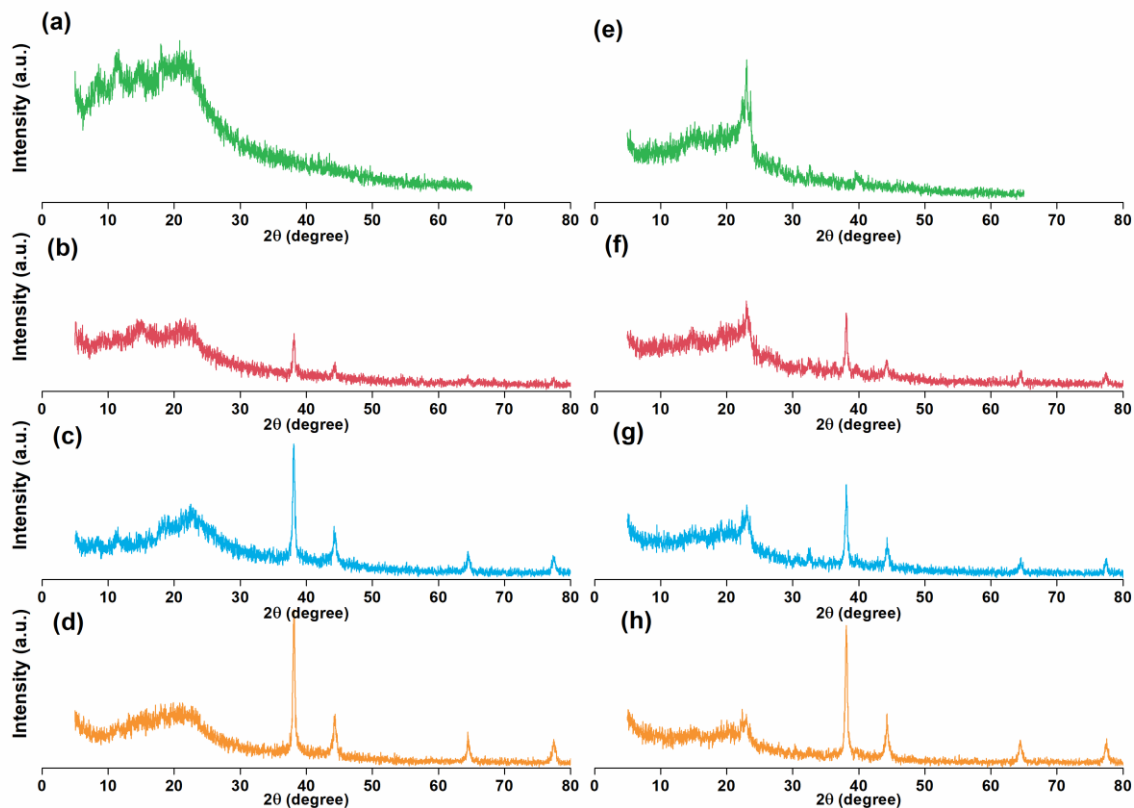


**Figure 5.1** XRD of (a) CS, (b) CSNA, (c) CSNB, (d) CSNC, (e) CP, (f) CPNA, (g) CPNB, and (h) CPNC matrices.

Figure 5.1 shows concentration-dependent XRD spectra of CSN and CPN matrices. The peaks in the case of concentration-dependent CSN evolved at  $38.1^\circ$ ,  $44.3^\circ$ ,  $64.5^\circ$  and  $77.4^\circ$  2-theta. These peaks are an evidence of distinguishing Bragg's reflections from the crystalline planes of the face-centred cubic lattice Ag NPs phase as (111), (200), (220) and (311) [5]. Similar crystalline peaks with negligible shifts appeared for concentration-dependent CPN matrices. In both the matrices, the presence of fundamental Bragg's reflection of CS and CP blend matrices (as discussed in section 3.2.1 of Chapter 3) are also persisted. However, the relative intensity of the polymer crystalline peaks decreased with an increase in Ag NPs concentration indicating an increase in the degree of an amorphous phase. These results are indicating the successful integration of Ag NPs in the respective matrices. On comparing the XRD spectra of equal Ag

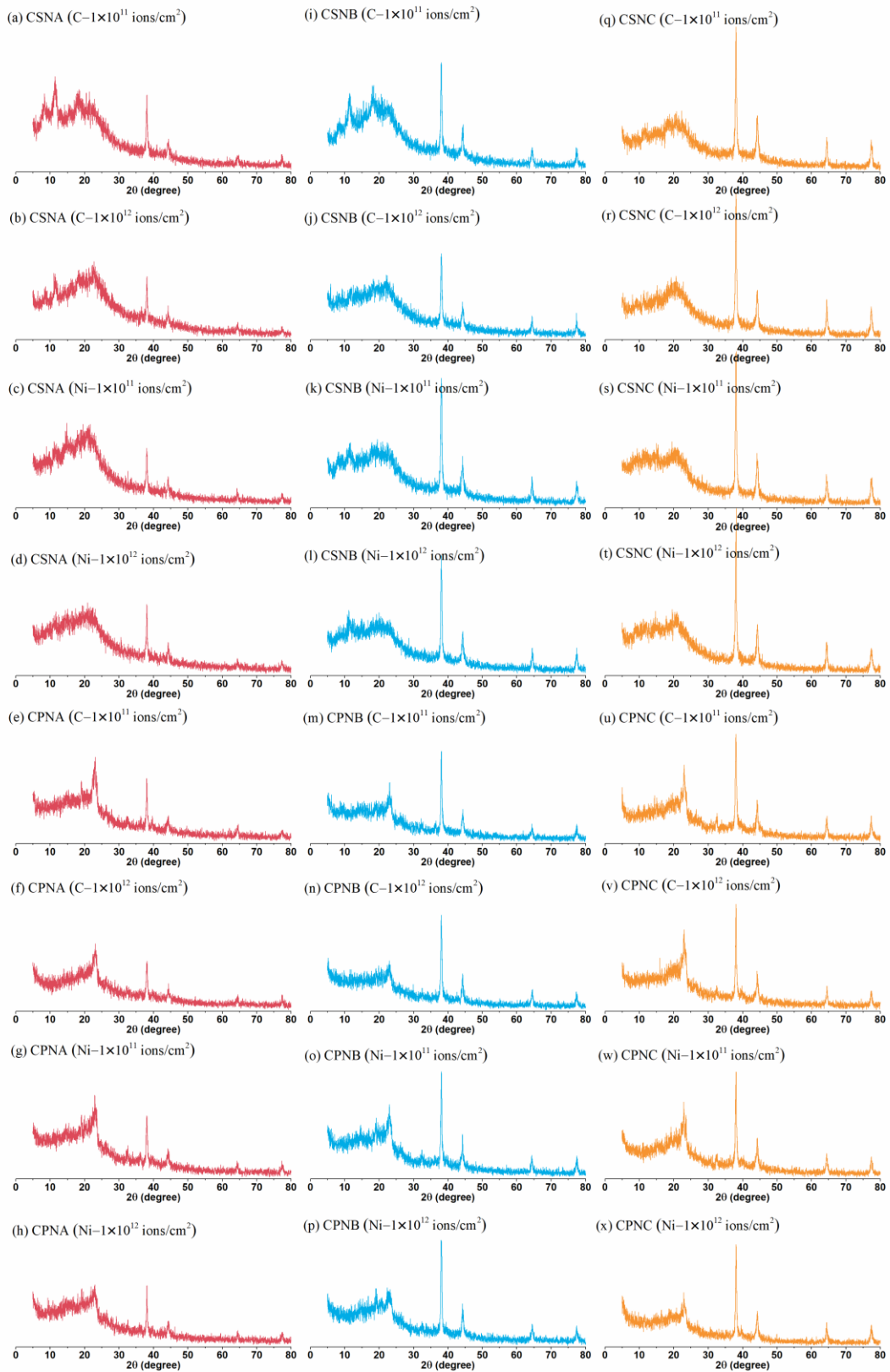


**Figure 5.2** XRD of (a-h) CSNA and CPNA, (i-p) CSNB and CPNB, and (q-x) CSNC and CPNC matrices irradiated with  $C^{+5}$  and  $Ni^{+7}$  ions at the fluence of  $1 \times 10^{11}$  and  $1 \times 10^{12}$  ions/cm<sup>2</sup>, respectively.

**Table 5.1** Variation in the crystallite size of pristine and irradiated CSN and CPN matrices with 60-MeV C<sup>+5</sup> and 100-MeV Ni<sup>+7</sup> ions at the fluence of 1×10<sup>11</sup> and 1×10<sup>12</sup> ions/cm<sup>2</sup>.

Sample	Crystallite Size (nm)				
	Pristine	C <sup>+5</sup> (1×10 <sup>11</sup> )	C <sup>+5</sup> (1×10 <sup>12</sup> )	Ni <sup>+7</sup> (1×10 <sup>11</sup> )	Ni <sup>+7</sup> (1×10 <sup>12</sup> )
CSNA	14.02	13.41	12.95	12.85	12.00
CSNB	15.58	15.27	14.58	15.13	13.81
CSNC	17.61	16.23	16.17	14.48	14.23
CPNA	19.93	18.15	16.83	16.26	15.78
CPNB	22.29	20.48	20.24	21.39	18.36
CPNC	22.56	22.50	22.46	22.35	22.27

NPs concentration revealed a relative change in intensity indicate the interaction of nanoparticles influenced by the structural properties of the host matrix. The dispersion of Ag NPs in the respective matrix considered at the molecular level could influence the separation, mobility and relaxation of the polymeric chain.

Figure 5.2 illustrates the effect of SHIs irradiation on CSN and CPN matrices with varying fluences. The peaks correspond to the polymer phase suppressed and become broader, indicating a decrease in the degree of polymer crystalline or semi-crystalline nature. Whereas the intensity of crystalline peak associated with Ag NPs moderately decreased. However, as an impact of MeV ions, the polymer assembly's localized structural feature of with Ag NPs convincingly modified. These structural amendments can be predicted by the crystallite size as obtained from the measured broadening ( $\beta_{1/2}$ ) of peaks was used in Scherrer equation [6] as inferred in Chapter 2 (section 2.4.1) and tabulated in Table 5.1. The crystallite size of CPN seems more than that of the CSN matrix showed an involvement of the crystalline phase of PEO. The crystalline size of CSN and CPN matrices decreased and revealed  $S_e$  and fluence dependent responses ascribed to disordering caused by MeV ions based on deposition of the abundant localized energy density into the polymeric assembly along the ion tracks [7].

### 5.2.2 ATR-FTIR Analysis

Figure 5.3 displays the Ag NPs concentration-dependent ATR-FTIR spectra of CSN matrices. Due to the incorporation of nanoparticles, the relative intensity of stronger overlapped O–H and N–H stretching modes evolved within the wavenumber regime of 3500–3300 cm<sup>-1</sup>

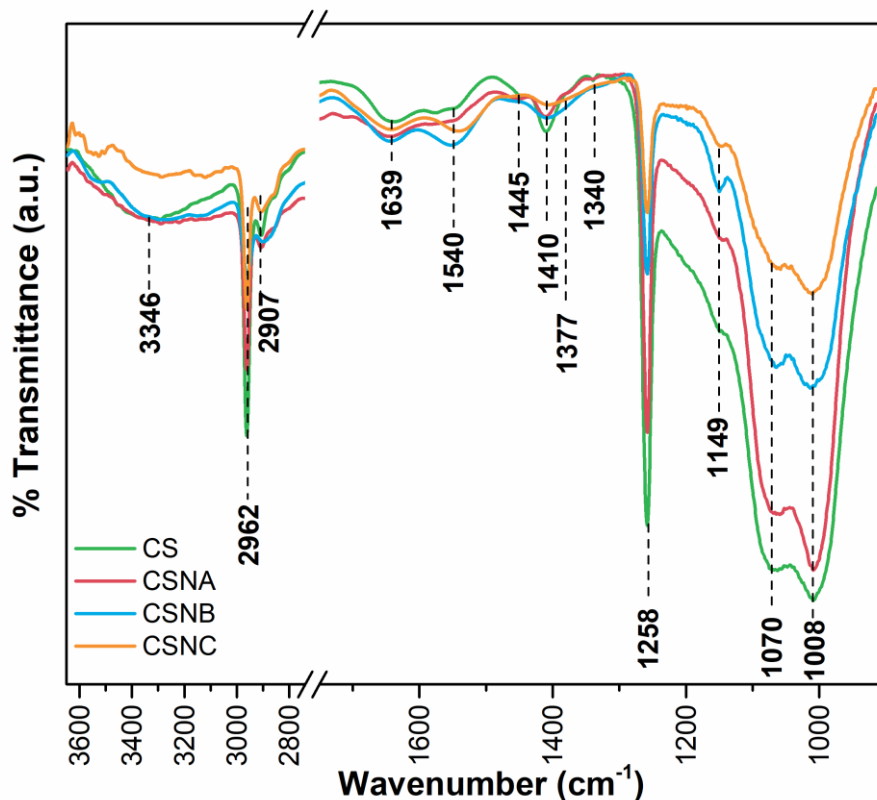


**Figure 5.3** FTIR spectra of concentration-dependent CSN matrices.

observed to be diminishing, which is evidence of Ag NPs affinity to N–H [8]. The band at  $1540\text{ cm}^{-1}$  assigned to ( $-\text{NH}_3^+$ ) shifted ( $\sim 8\text{ cm}^{-1}$ ) because of the formation of linkages on the surface of Ag NPs due to the availability of excess protons. Broadening and shifting toward lower wavenumber side with waning in intensity due to Ag NPs incorporating have been remarked in literature [5,9]. The bands at  $1377$  (symmetric  $\text{CH}_3$  deformation and CH bending),  $1340$ , and  $1445\text{ cm}^{-1}$ , merged with  $1410\text{ cm}^{-1}$ . The  $1410\text{ cm}^{-1}$  ( $\text{CH}_2$  bending and  $\text{CH}_3$  deformation) shifted toward the lower wavenumber region. The vibrational mode associated with glucose rings of CS at  $1149\text{ cm}^{-1}$  becomes intense and broader.

Figure 5.4 shows the Ag NPs concentration-dependent ATR-FTIR spectra of CPN matrices. A distinctive discrepancy in CSN matrices is observed in comparison with CPN vibrational modes. Like CSN matrices, the hydrogen-bonded O–H and N–H groups, as perceived across the  $3000\text{--}3600\text{ cm}^{-1}$  wavenumber are immensely diminished [10]. The vibrational mode for CS observed at  $1540\text{ cm}^{-1}$  (NH bending (amide II)) is shifted ( $\sim 20\text{ cm}^{-1}$ ) to lower wavenumber side. The modes at  $1636\text{ cm}^{-1}$  and  $1258\text{ cm}^{-1}$  assigned to C=O stretching (amide I) and OH

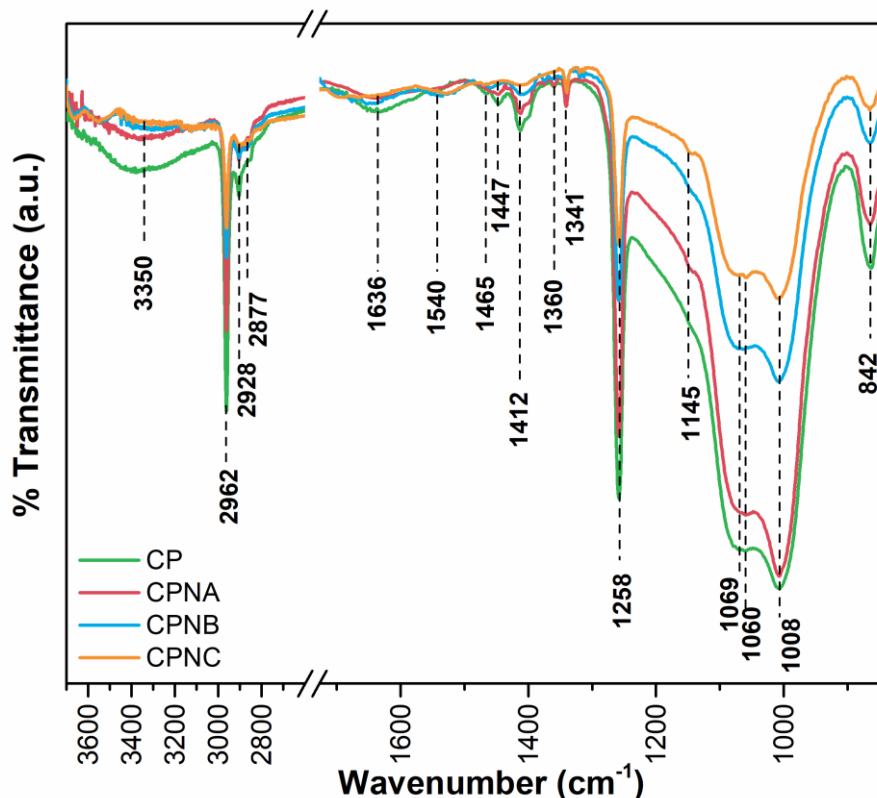


**Figure 5.4** FTIR spectra of concentration-dependent CPN matrices.

bending, respectively, seem to be suppressed. The relative intensity of vibrational modes at 1069 and 1008  $\text{cm}^{-1}$  ascribed to CS's saccharide feature is also diminished. The 1412  $\text{cm}^{-1}$  ( $\text{CH}_2$  bending and  $\text{CH}_3$  deformation) shifted ( $\sim 6 \text{ cm}^{-1}$ ) to the lower wavenumber side. The mode appeared at 1145  $\text{cm}^{-1}$  assigned to glucose rings of CS is intensify. Whereas the signature vibrational modes of PEO are also suppressed. However, there is a moderate change in peak intensity of 1060  $\text{cm}^{-1}$  (C–O–C stretching), 1341  $\text{cm}^{-1}$  ( $\text{CH}_2$  wagging) and 842  $\text{cm}^{-1}$  ( $\text{CH}_2$  rocking) modes assigned to PEO [11] in comparison with vibrational modes of CS. Also, the peak position of this mode does not shift. The shift in peak position and amendment in peak intensity implying that  $-\text{NH}_2$  and  $-\text{OH}$  groups of CS as well as C–O–C group PEO, remarkably interact with Ag NPs. However, Ag NPs moderates the interaction between CS and PEO on account of the prominent contribution of amine, hydroxyl and ether groups to the interaction with silver NPs [12].

In both cases, the presence of Ag NPs constrains the interactions among main and side-chain functional groups. Indeed, the abundant availability of excess proton facilitates

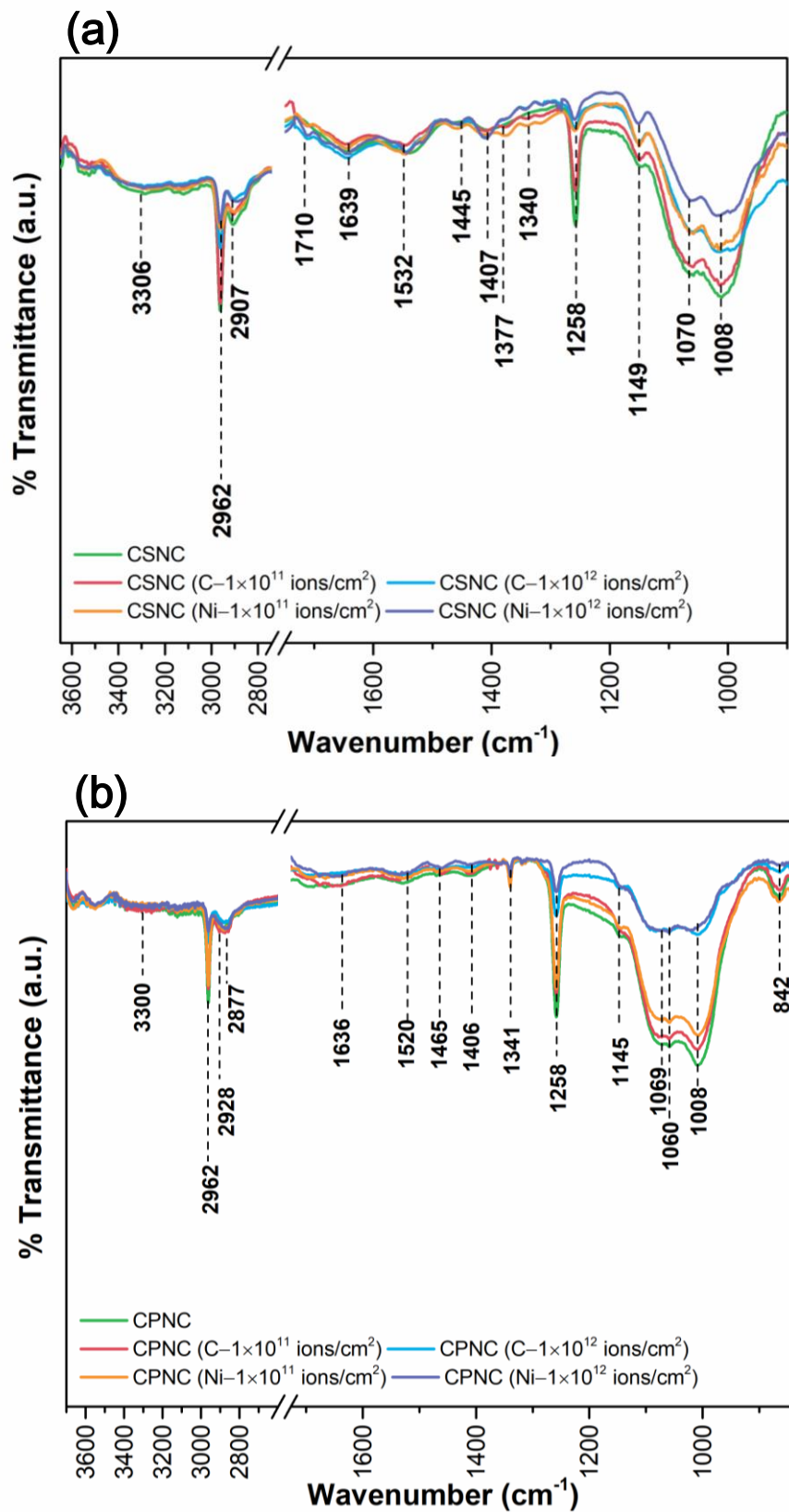


**Figure 5.5** FTIR spectra of (a) CSNC (b) CPNC matrices irradiated with  $C^{+5}$  and  $Ni^{+7}$  ions at the fluences of  $1 \times 10^{11}$  and  $1 \times 10^{12}$  ions/cm<sup>2</sup>, respectively.

hydrogen bonding due to dipolar coupling between the surface charge of Ag NPs and proton in CS. The change in vibrational mode relevant to glucose rings implying defects formation *via* charge transfer reaction between Ag NPs and CS. The adjacent polymeric coating on the nanoparticle surface restricts the mobility of macromolecular chains. Therefore, the nanoparticles within the polymeric assembly caused confining effects [13].

Figure 5.5(a) and Figure 5.5(b) revealed the fluence-dependent effect of  $C^{+5}$  and  $Ni^{+7}$  ions irradiation on CSNC and CPNC matrices' vibrational modes, respectively. For both the matrices, the vibrational modes appeared at  $2907\text{ cm}^{-1}$  (asymmetric C–H stretching),  $1258\text{ cm}^{-1}$  (–OH bending) as well as  $1070\text{ cm}^{-1}$  (glucose rings),  $1008\text{ cm}^{-1}$  (glycosidic linkage) and  $1060\text{ cm}^{-1}$  (C–O–C stretching) are remarkably suppressed. Therefore, an atomic ratio of hydrogen to carbon (H/C) declined upon SHIs irradiation due to polymer degradation. The macromolecular degradation occurred *via* rupture of numerous polymeric linkages and the formation of low-molecular species associated with the degassing of some volatile products [7]. Consequently, a newer carbonyl band developed at  $1710\text{ cm}^{-1}$  for CSN matrices, as seen from Figure 5.5(a). Although, the carbonyl band does not grow in the case of irradiated CPN matrices. This is revealed to the mutual stabilizing effect of coexisting binary polymeric systems. While the vibrational modes in the range of  $3500\text{--}3000\text{ cm}^{-1}$  and  $1540\text{ cm}^{-1}$  associating with  $-\text{NH}_2$  groups are moderately changed upon SHIs irradiation. This implied a stronger affinity of amine groups in the confining effects of NPs.

### 5.2.3 Optical Analysis

Figure 5.6(a) and Figure 5.6(b) illustrate Ag NPs concentration-dependent UV-Visible absorption spectra of CSN and CPN matrices, respectively. The optical response of metallic nanoparticles strongly relies on profiles of particle (i.e. dimensions, shape, surface feature), composition, adjacent medium, separation among particles, etc. [14]. Surface plasmon resonance (SPR) peak originated at around 410 nm is evidence of silver nanoparticles within the assembly of polymeric matrices [8,15]. A broader and asymmetric shape of SPR peak for CSN and CPN matrices with a prolonged tail observed from Figure 5.6(a) and Figure 5.6(b). The nature of the SPR peak revealed multipolar excitations and radiative damping due to elevated concentration of Ag NPs with variable-sized dispersion. The coherent excitation of

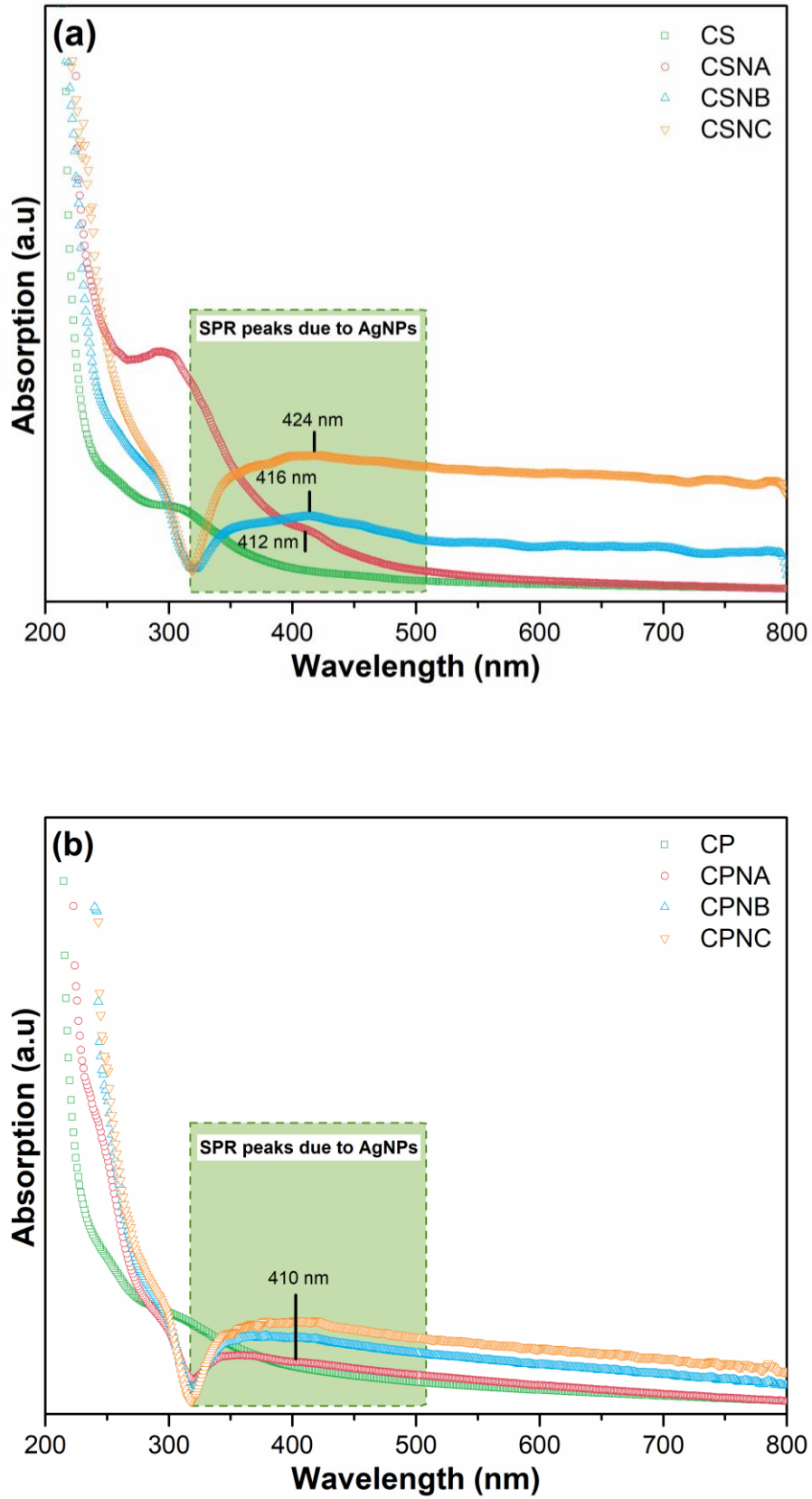


**Figure 5.6** UV-Visible spectra of concentration-dependent (a) CSN and (b) CPN matrices, respectively.

the nanoscale constitute and its surrounding dielectric medium excite the electrons [16]. These excited electrons govern the intensity of the SPR peak.

Figure 5.7(a) and Figure 5.7(b) show the UV-Visible absorption spectra of  $C^{+5}$  and  $Ni^{+7}$  ions irradiated CSN and CPN matrices at the fluence of  $1 \times 10^{11}$  and  $1 \times 10^{12}$  ions/cm<sup>2</sup>, respectively. The SPR peak exhibited a successive redshift as the ion fluence increased for both the matrices. An amendment in the optical response contributed from both the polymeric system and nanoparticles, that is, improvement in dielectric constant and redistribution of Ag NPs, respectively [17]. Indeed, the scattering effect of electron and the charge transfer process occurred at the NPs surface govern by the particle-polymer interface features [18]. Hence, reform in the particle-polymer interface is reflected in the optical properties of the polymer

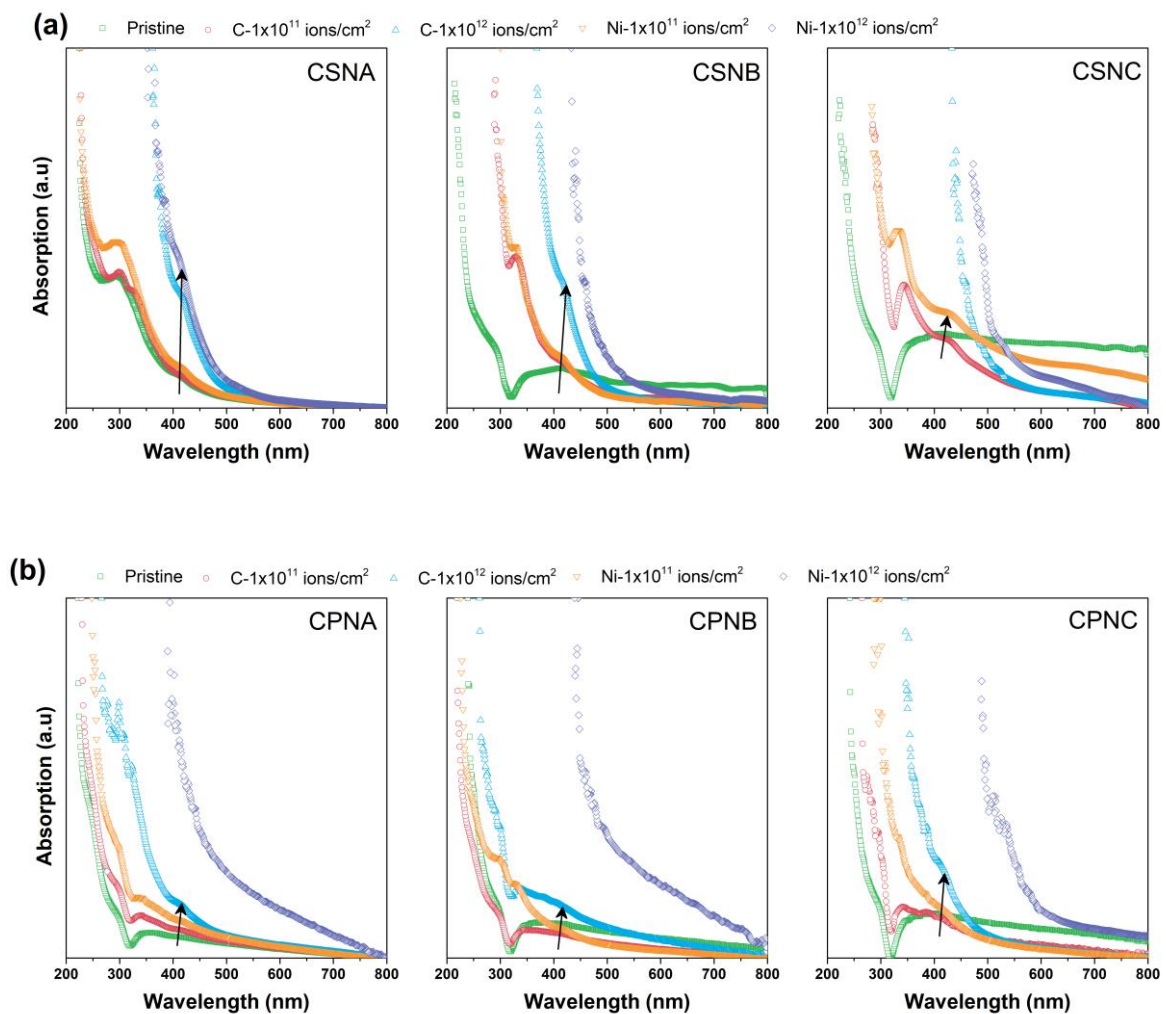


**Figure 5.7** UV-Visible spectra of (a) CSN (b) CPN matrices irradiated with  $C^{+5}$  and  $Ni^{+7}$  ions at the fluences of  $1 \times 10^{11}$  and  $1 \times 10^{12}$  ions/cm<sup>2</sup>, respectively.

**Table 5.2 Variation in optical energy bandgap ( $E_g$ ), the number of carbon atoms per conjugation length (N) and ( $R^2$ ) of pristine and irradiated CSN and CPN matrices with 60-MeV  $C^{+5}$  and 100-MeV  $Ni^{+7}$  ions at the fluence of  $1 \times 10^{11}$  and  $1 \times 10^{12}$  ions/cm<sup>2</sup>.**

Sample	$C^{+5}$ (60 MeV)			$Ni^{+7}$ (100 MeV)		
	$E_g$ (eV)	N	$R^2$	$E_g$ (eV)	N	$R^2$
Pristine CSNA	$5.01 \pm 0.02$	47	0.97	$5.01 \pm 0.02$	47	0.97
CSNA ( $1 \times 10^{11}$ ions/cm <sup>2</sup> )	$4.83 \pm 0.04$	51	0.90	$4.59 \pm 0.04$	56	0.98
CSNA ( $1 \times 10^{12}$ ions/cm <sup>2</sup> )	$3.22 \pm 0.01$	113	0.84	$3.11 \pm 0.02$	121	0.93
Pristine CSNB	$4.89 \pm 0.02$	49	0.96	$4.89 \pm 0.02$	49	0.96
CSNB ( $1 \times 10^{11}$ ions/cm <sup>2</sup> )	$3.92 \pm 0.01$	77	0.99	$3.77 \pm 0.01$	83	0.99
CSNB ( $1 \times 10^{12}$ ions/cm <sup>2</sup> )	$3.20 \pm 0.01$	115	0.96	$2.69 \pm 0.01$	162	0.85
Pristine CSNC	$4.65 \pm 0.02$	54	0.96	$4.65 \pm 0.02$	54	0.96
CSNC ( $1 \times 10^{11}$ ions/cm <sup>2</sup> )	$3.87 \pm 0.01$	79	0.97	$3.56 \pm 0.04$	93	0.88
CSNC ( $1 \times 10^{12}$ ions/cm <sup>2</sup> )	$2.70 \pm 0.01$	162	0.92	$2.41 \pm 0.01$	203	0.92
Pristine CPNA	$4.57 \pm 0.01$	56	0.99	$4.57 \pm 0.01$	56	0.99
CPNA ( $1 \times 10^{11}$ ions/cm <sup>2</sup> )	$4.48 \pm 0.01$	59	0.97	$4.28 \pm 0.02$	64	0.93
CPNA ( $1 \times 10^{12}$ ions/cm <sup>2</sup> )	$3.80 \pm 0.05$	81	0.87	$2.83 \pm 0.02$	147	0.84
Pristine CPNB	$4.36 \pm 0.02$	62	0.94	$4.36 \pm 0.02$	62	0.94
CPNB ( $1 \times 10^{11}$ ions/cm <sup>2</sup> )	$4.27 \pm 0.02$	65	0.94	$3.92 \pm 0.01$	77	0.96
CPNB ( $1 \times 10^{12}$ ions/cm <sup>2</sup> )	$3.77 \pm 0.04$	83	0.93	$2.56 \pm 0.02$	180	0.96
Pristine CPNC	$4.12 \pm 0.01$	69	0.98	$4.12 \pm 0.01$	69	0.98
CPNC ( $1 \times 10^{11}$ ions/cm <sup>2</sup> )	$3.86 \pm 0.01$	79	0.99	$3.82 \pm 0.01$	81	0.98
CPNC ( $1 \times 10^{12}$ ions/cm <sup>2</sup> )	$2.66 \pm 0.01$	166	0.81	$2.45 \pm 0.01$	196	0.98

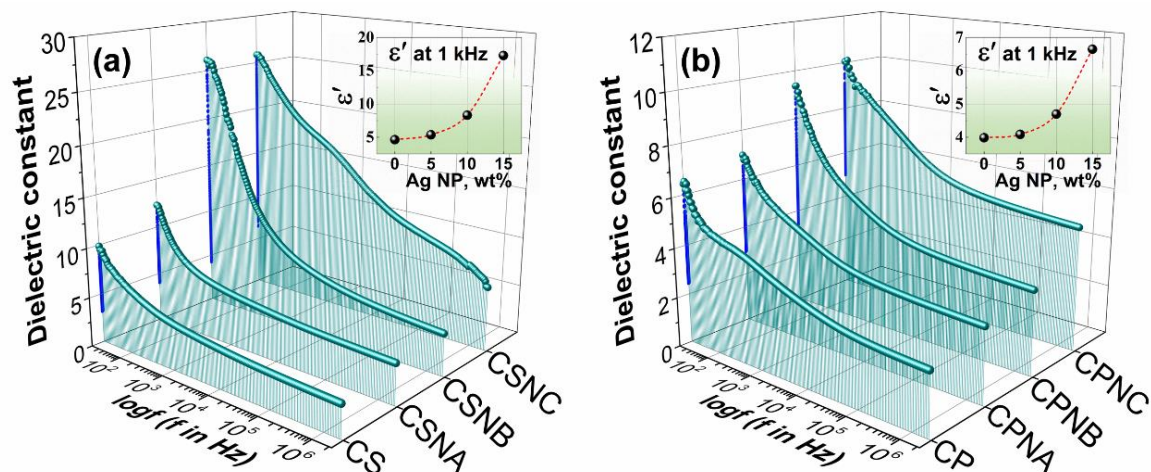
nanocomposites matrices. The setup of the polymeric layer around the surface of nanoparticles, that is, polymer grafting, may build up the effective volume of the nanoparticles and restrict the mobility of the polymer chain and the nanoparticles. The grafting of polymer is enhanced upon SHIs irradiation caused by tremendous electronic energy loss of MeV ions. Which is ascribed to the reordering of polymeric materials as a result of the rapid cool-down process of the molten phase of polymer [7,19].

The peak evolved within a wavelength regime of 300 to 350 nm indicating chromophores' formation (see Figure 5.7(a-b)) for both CSN and CPN matrices upon MeV ions irradiation. It is also observed that the SHIs yielded reformation in AE shape and monotonic redshift as a function of ion fluence. An amendment in the AE is attributed to the formation of defects, explicitly, randomization of polymeric chain and wrecking of vital linkages [7]. Whereas the persistent redshift of AE indorsed to the instigation of lower molecular-weight species and ions, that is, improved charge carrier density. Also, outgassing of volatile molecular fragments of various species upon MeV ions irradiation [19].

The AE variation is reflected in the optical bandgap ( $E_g$ ) of CSN and CPN matrices. The bandgap of pristine and MeV ions irradiated matrices were estimated using Tauc's approach, as discussed in section 2.4.3 of Chapter 2.  $E_g$ 's calculated value of for CSNA, CSNB and CSNC is 5.01 eV, 4.89 eV and 4.65 eV, respectively. Whereas the corresponding value for CPNA, CPNB and CPNC matrices is found to be 4.57 eV, 4.63 eV and 4.12 eV, respectively. A decrease in electron transition energy upon Ag NPs loading is indorsed to the configuration of charge transfer complexes between the HOMO and LUMO energy bands. From Table 5.2, the wide bandgap of CSN and CPN can be engineered using suitable beam parameters as a result of the formation of new energy levels (traps) between the HOMO and LUMO band. Indeed, MeV ions induced change in optical response is due to the generation of unsaturation and structural reform of  $sp^3$  and  $sp^2$  [19,20]. Compagnini *et al.* [21] revealed that the polymeric system's optical properties govern by the atomic ratio of hydrogen to carbon (H/C). A decrease in bandgap upon irradiation corresponds to low H/C concentration. This is collaborated with substantial breaking of C–H and –OH coordinates, as demonstrated in section 5.2.2. In the present case,  $sp^3$  to  $sp^2$  hybridization facilitates carbonaceous clustering. The number of carbon atoms per conjugation length (N) was evaluated by employing the Fink model as explained in section 2.4.3 of Chapter 2 and tabulated in Table 5.2. The carbon-rich matrices have been developed because of substantial hydrogen gas liberation, subsequently, altering the surrounding environments of the NPs. Which in turn affects the dielectric constant may responsible for a monotonic red shift [22]. The remarkable red shift of AE and bandgap tunability as a function of beam parameters denotes that the CSN and CPN are suitable materials that can be utilized as UV shielding and bandgap tuner to advance the optical devices.

### 5.2.4 AC Electrical Frequency Response

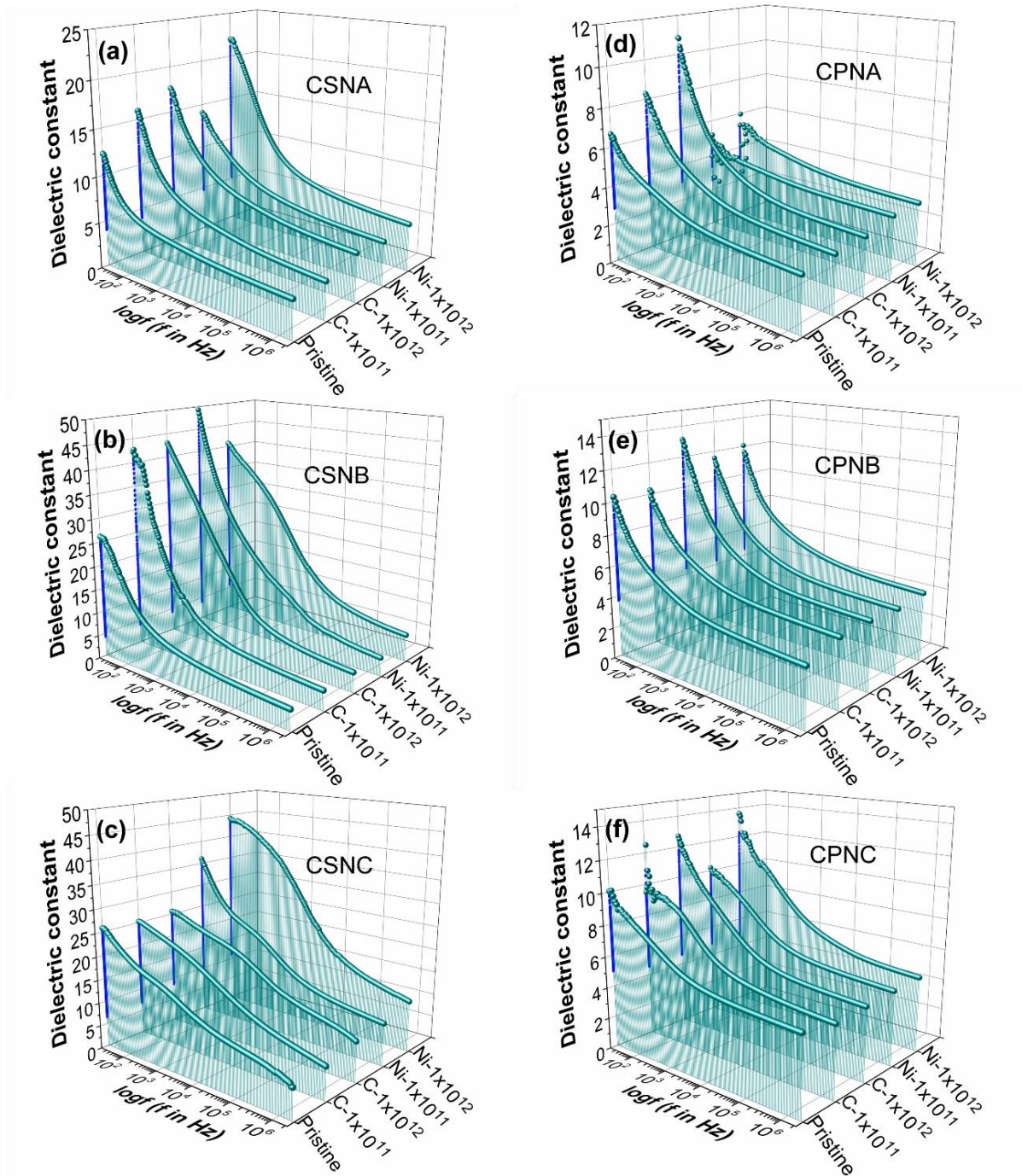
Frequency-dependent dielectric spectroscopy is a versatile technique to avail prominent evidence about polymer specimens' internal behavior of with nano-filler because of prevailing the distinctive phases [23]. The MeV ions interaction with polymer nanocomposites matrices were indefinitely influenced the macromolecular dynamics and conduction mechanism. Former macroscopic techniques could not perceive such changes. Hence, distinctive dielectric formalisms were employed to evaluate and explore the MeV ions induced amendments. The variation of dielectric constant as a function of log frequency for CSN and CPN matrices is shown in Figure 5.8. These matrices involving constitutes of distinct phases with diversity in



**Figure 5.8** Plot of dielectric constant versus log frequency of Ag NPs dependent (a) CSN and (b) CPN matrices, respectively. Inset depict the variation of  $\epsilon'$  at 1 kHz versus Ag NPs wt% for CSN and CPN matrices.

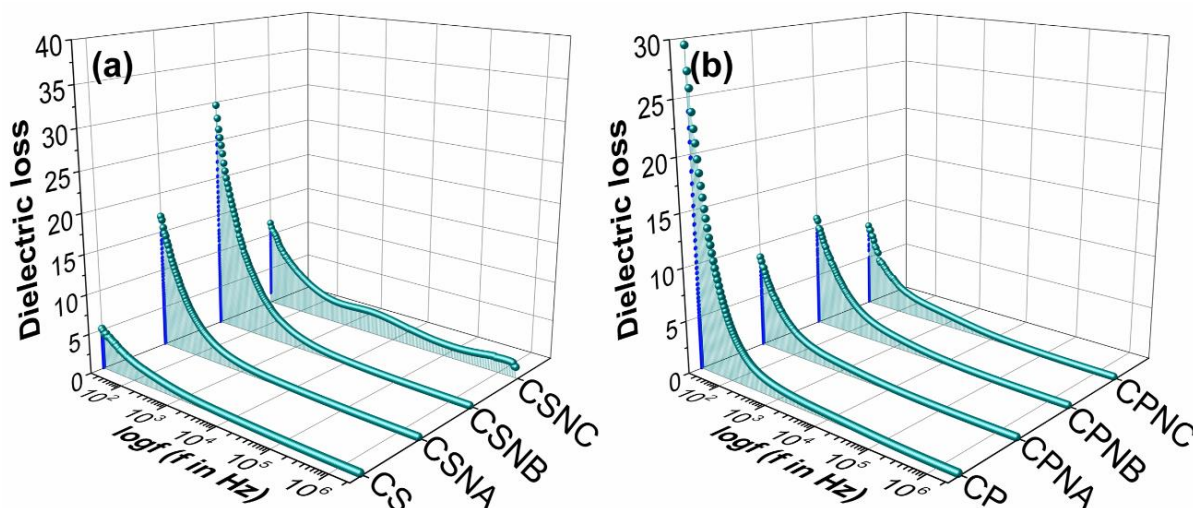
conductivity. In polymer nanocomposites matrices, metallic islands of NPs existed in an insulating host. The interfacial dipole is formed at the interface due to partial charge charge transfer [18]. Therefore, the dielectric constant solely increases with increasing Ag NPs concentration, as perceived from Figure 5.8. The  $\epsilon'$  values of CSNA and CSNB matrices exhibited frequency-independent response over 40 kHz to 2 MHz, while CSNC showed except frequency-dependent response over the entire frequency range. Simultaneously, there is a quick and rapid increase as frequency decrease from 40 kHz to 20 Hz observed for CSN matrices from Figure 5.8(a). Figure 5.8(b) revealed that CPN matrices showed a frequency-independent response over 20 kHz to 2 MHz. At the same time, there is a slow and gradual increase with a decrease in frequency from 20 kHz to 20 Hz. Inset of Figure 5.8(a) and Figure 5.8(b) revealed a non-linear increase in  $\epsilon'$  as a function of Ag NPs wt% for CSN and CPN matrices at the fixed frequency of 1 kHz. The rise in  $\epsilon'$  at 1 kHz is about 272% and 66% with 15% of Ag NPs loading in CS and CP blend, respectively.

Figure 5.9 depicts the variation of dielectric constant ( $\epsilon'$ ) as a function of log frequency for pre and post  $C^{+5}$  and  $Ni^{+7}$  ions irradiated CSN and CPN matrices at the fluence of  $1 \times 10^{11}$  and  $1 \times 10^{12}$  ions/cm<sup>2</sup>. The values of  $\epsilon'$  increases over the entire frequency region with fluence for both the ions. The rise in  $\epsilon'$  upon  $Ni^{+7}$  irradiation is more abrupt, indicating the charge carriers' formation is more than  $C^{+5}$  irradiation. Also, increased lower frequency dispersion upon irradiation is attributed to the increased contribution of electrode polarization effects [24]. The properties of materials were significantly transformed due to grafting of polymer with nano-



**Figure 5.9** Plot of dielectric constant versus log frequency for (a) CSNA, (b) CSNB, (c) CSNC, (d) CPNA, (e) CPNB, and (f) CPNC matrices irradiated with  $C^{+5}$  and  $Ni^{+7}$  ions at the fluence of  $1 \times 10^{11}$  and  $1 \times 10^{12}$  ions/cm<sup>2</sup>, respectively.

sized materials, which is governed by the size, surface and confining effects of nanomaterial. Biswas *et al.* [25] demonstrated the silver nanocluster's reordering within carbonaceous nanoregions in a polymeric host. They reveal tailoring of nanoparticles shape and size located on the surface and residing in the polymer matrix. The prior studies carried out by our group with the objective of SHIs effect on the physical properties of PS-Ag NPs [26] and PMMA-

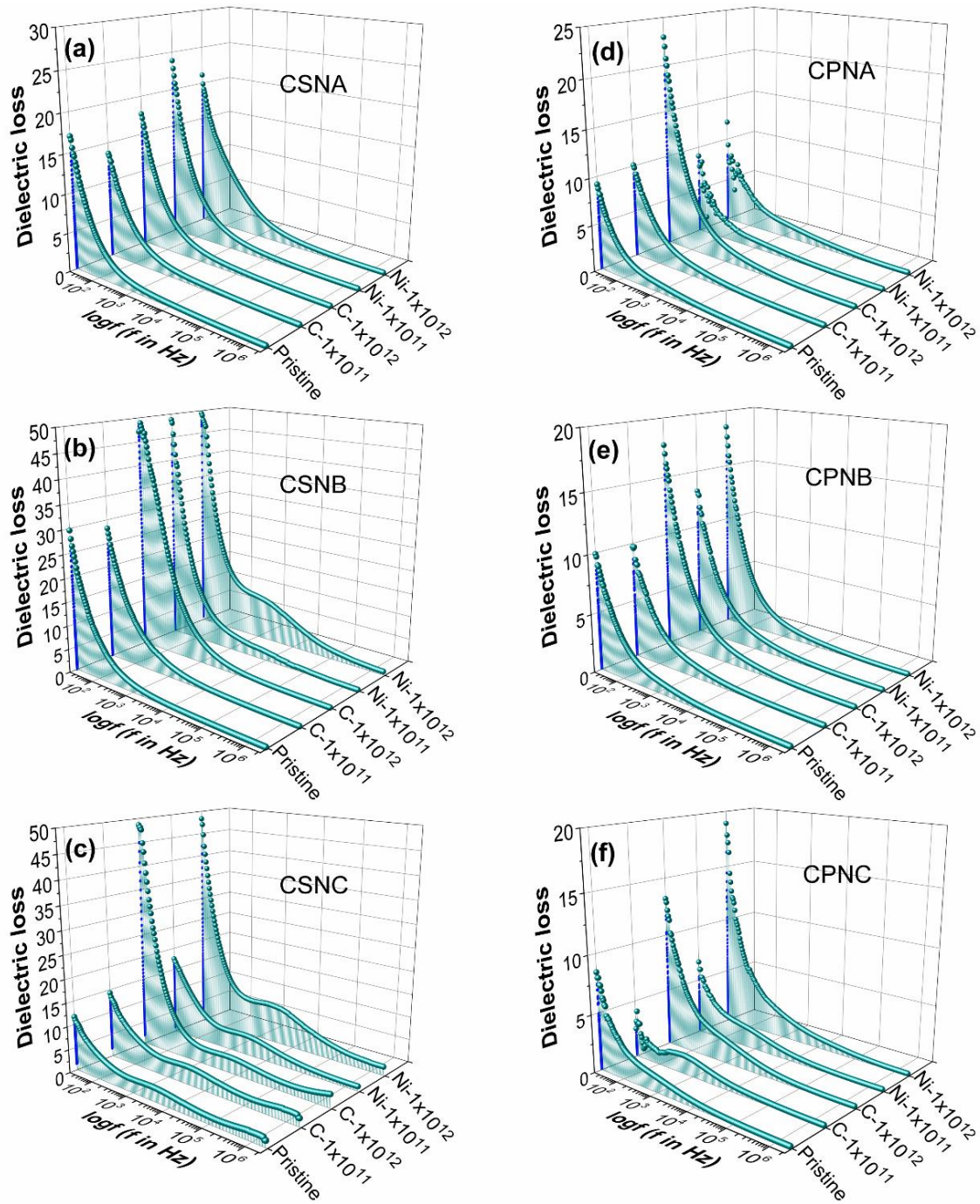


**Figure 5.10** Plot of dielectric loss versus log frequency of Ag NPs dependent (a) CSN and (b) CPN matrices, respectively

Ag NPs [27] revealed that the physicochemical amendments may be facilitated cluster-to-cluster interaction due to increase in correlation length. These studies validate the discussions of MeV ions induces modified response of dielectric constant for CSN and CPN matrices.

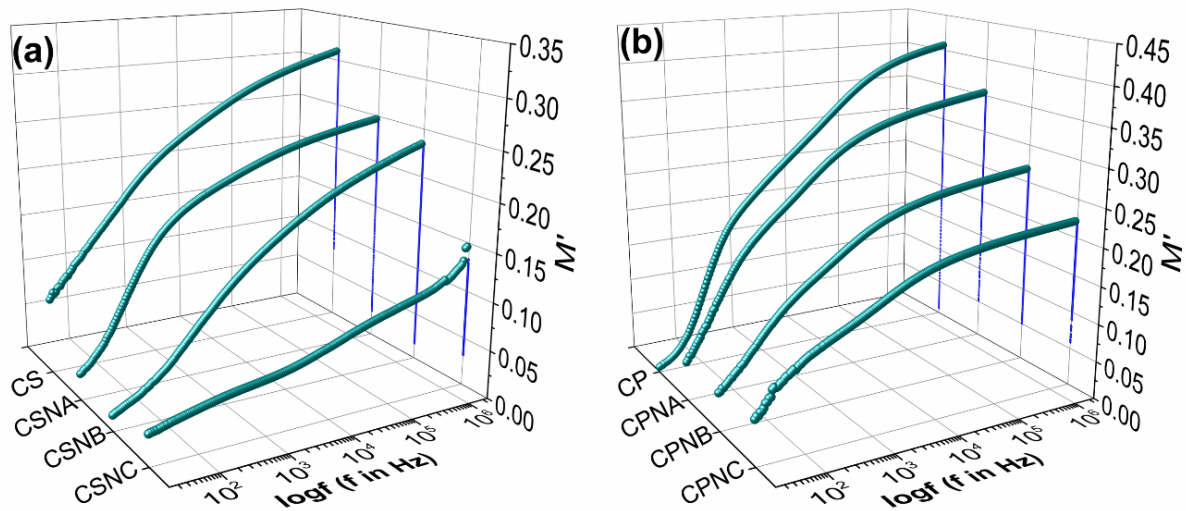
The variation of dielectric loss ( $\epsilon''$ ) as a function of log frequency for CSN and CPN matrices is shown in Figure 5.10. The dielectric loss increases monotonically with decreasing frequency ascribed to the interfacial polarization mechanism of the heterogeneous system [27]. Whereas the frequency region below 1 kHz is attributed to the dc conductivity behavior obeying the relation,  $\epsilon'' \propto f^{-1}$ . Except, minor relaxation in the frequency range 1 kHz to 20 kHz for the CSNC matrix. Also, the exponent nature of the dielectric loss spectra indicates the dominant of polarization effect over the dc conductivity [28].

Figure 5.11 represents the variation of dielectric constant ( $\epsilon'$ ) as a function of log frequency for pre and post  $C^{+5}$  and  $Ni^{+7}$  ions irradiated CSN and CPN matrices at the fluence of  $1 \times 10^{11}$  and  $1 \times 10^{12}$  ions/cm<sup>2</sup>. It is noticed that the values of  $\epsilon'$  increases across the overall frequency range with increasing fluence. Also, a moderate rise in  $\epsilon'$  upon MeV ions irradiation is noticed for CPN matrices concerning CSN matrices. However, a small relaxation peak within 1 kHz to 20 kHz frequency span upon SHIs irradiation is perceived for certain fluence. This kind of strange response is attributed to the release of the frozen dipoles due to the scission of the macromolecule chain and their cooperative movement with the adjacent polymer segment.



**Figure 5.11** Plot of dielectric loss versus log frequency for (a) CSNA, (b) CSNB, (c) CSNC, (d) CPNA, (e) CPNB, and (f) CPNC matrices irradiated with  $C^{+5}$  and  $Ni^{+7}$  ions at the fluence of  $1 \times 10^{11}$  and  $1 \times 10^{12}$  ions/cm<sup>2</sup>, respectively.

As explained in section 2.4.4 of Chapter 2 that there is an inverse relationship between complex electrical modulus ( $M^*$ ) and complex dielectric permittivity ( $\epsilon^*$ ) [23,24,29,30]. The electric modulus formalism is an ingenious approach indorse to study the relaxation phenomenon by suppressing the low frequency electrode/interfacial polarization effect [24]. The polymer-metal nanocomposites matrices are disorder in nature and may exhibit various overlapped

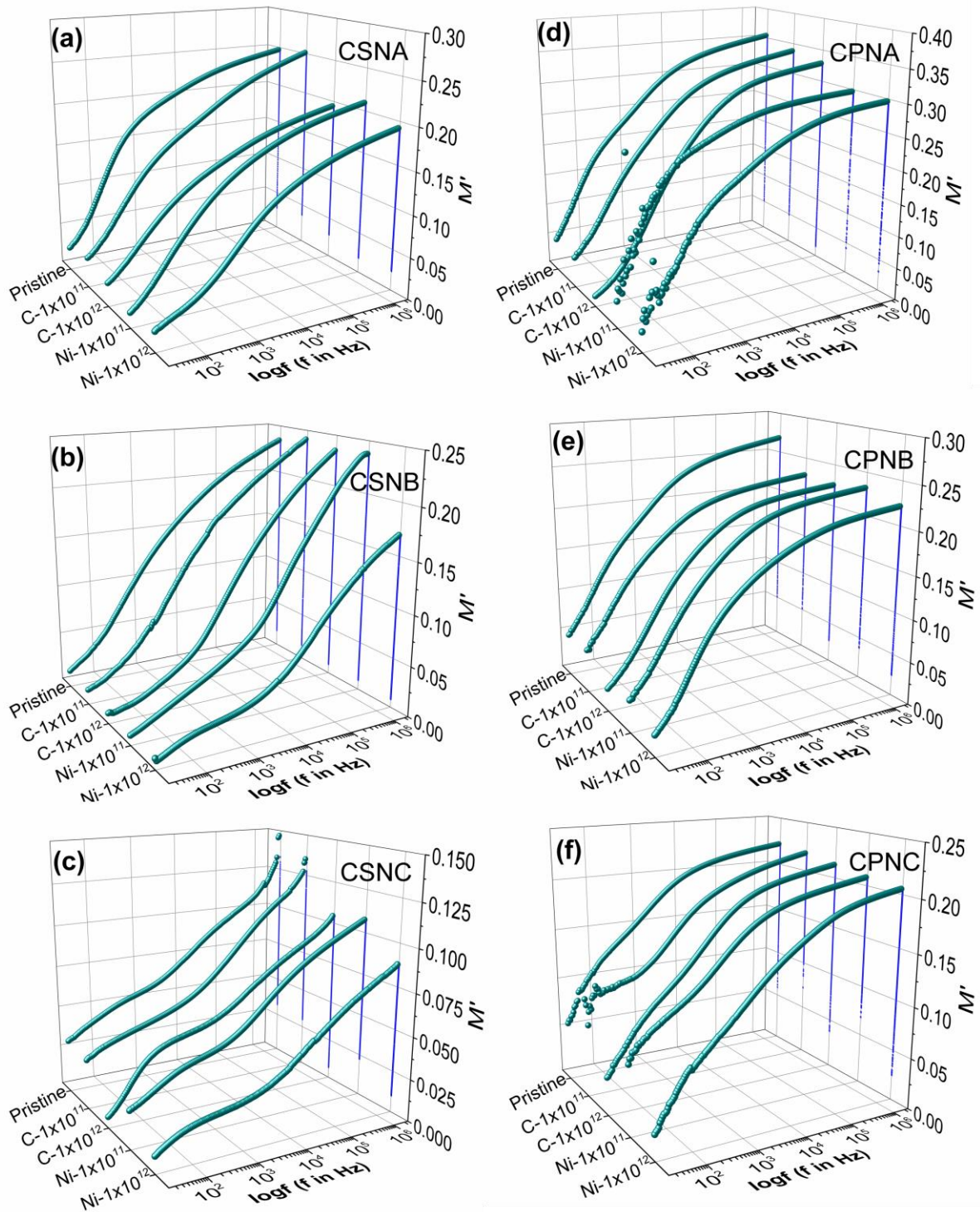


**Figure 5.12** Plot of real part of electric modulus versus log frequency of Ag NPs dependent (a) CSN and (b) CPN matrices, respectively.

relaxation processes, which can be explored and distinguishable through the electric modulus analysis.

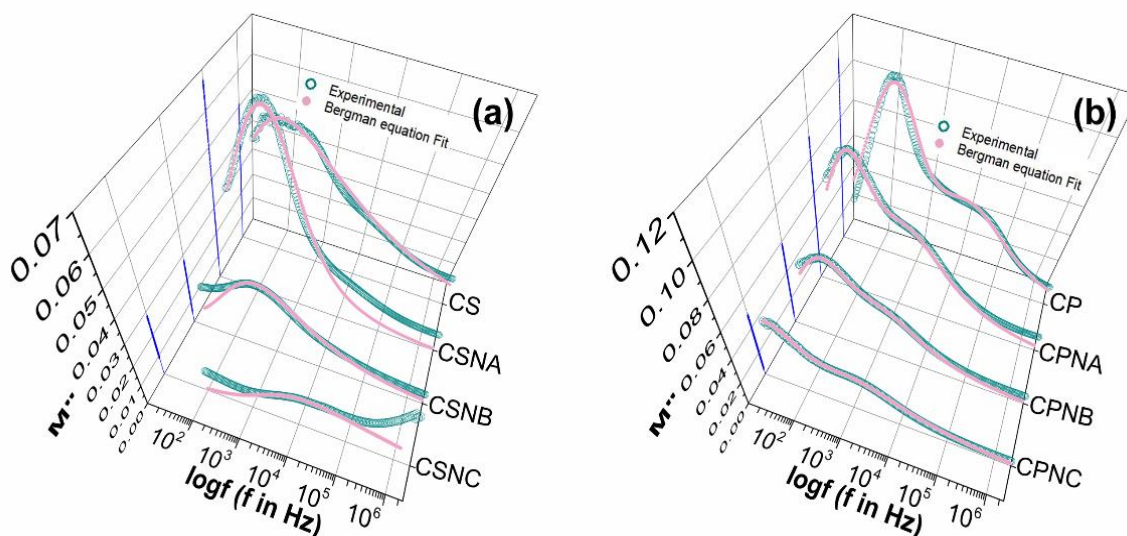
Figure 5.12 shows the variation of real part of electric modulus ( $M'$ ) as a function of log frequency for CSN and CPN matrices. It is perceived that the frequency-dependent values of  $M'$  decreased monotonically with the increasing Ag NPs loading for CSN and CPN matrices. At low frequency window, the graphics of  $M'$  tends to reasonably trivial. The values of  $M'$  increase asymptotically with increasing frequency and tend to level off by reaching a maximum value ( $M_{\infty}=1/\epsilon_{\infty}$ ) at higher frequency. The frequency-dependent  $M'$  seem to be reduced over the entire range of frequency with increasing Ag NPs loading.

Figure 5.13 illustrates the variation of the real part of electric modulus as a function of log frequency for pre and post  $C^{+5}$  and  $Ni^{+7}$  ions irradiated CSN and CPN matrices at the fluence of  $1 \times 10^{11}$  and  $1 \times 10^{12}$  ions/cm<sup>2</sup>. Analogous to the Ag NPs dependent response of CSN and CPN matrices, the  $M'$  spectra upon MeV ions irradiation also exhibits a decreasing tendency as a function of fluence throughout the frequency range. This may be ascribed to constrained polymeric chains within a narrow space due to high Ag NPs doping accompanied by polymeric degradation yielding isolated behavior of the macromolecules at the nanoscale extent. The response of  $M'$  at lower frequency is indorsed to the suppression of dispersion owing to interfacial/electrode electric double-layer polarization [23]. At the same time, the high-



**Figure 5.13** Plot of real part of electric modulus versus log frequency for (a) CSNA, (b) CSNB, (c) CSNC, (d) CPNA, (e) CPNB, and (f) CPNC matrices irradiated with  $C^{+5}$  and  $Ni^{+7}$  ions at the fluence of  $1 \times 10^{11}$  and  $1 \times 10^{12}$  ions/cm<sup>2</sup>, respectively.

frequency saturation is ascribed to the dispersion of conductivity relaxation in a broad span of frequencies [31]. Indicating a consequence of the characteristic relaxation phenomenon



**Figure 5.14** Plot of imaginary part of electric modulus versus log frequency of Ag NPs dependent (a) CSN and (b) CPN matrices, respectively.

involving a loss peak in the imaginary part of electric modulus spectra.

The imaginary electric modulus spectra ( $M''$ ) as a function of frequency for CSN and CPN matrices is presented in Figure 5.14, confirms well-resolved peaks ascribed to the phenomena of relaxation processes. The graphics of  $M''$  reveal a solely single relaxation phenomenon for CSN, while two different relaxation phenomena for CPN. For the case of CSN, as discussed in the ATR-FTIR section, the confined effect of nanoparticle indicating the hydrogen bonding and weaken the interactions among the main and side-chains of polymeric functional groups. As a result, with increasing the Ag NPs loading peak of  $M''$  spectra is shifting towards the high-frequency side. The shape of relaxation peak, that is, peak value ( $M''_{max}$ ) and peak broadening, is also remarkably amended. The relaxation observed in the window of ( $f < f_{max}$ ) is indorsed to the existence of interfacial polarization plus long-range migration of charge carriers, explicitly, efficient hopping between the adjacent sites [31]. The relaxation for frequencies ( $f > f_{max}$ ) indorsed to the short-range drift of charge carriers within potential wells [32]. For the case of CPN matrices, two distinct relaxation phenomena in  $M''$  spectra is perceived due to the coexistence of semi-crystalline and amorphous phase in the CP blend, as we have discussed in section 3.2.4 of Chapter 3. Upon embedding the Ag NPs, both relaxation peaks shifted to lower frequency concerning the CP blend. Indeed, there is a rearrangement of the main chain and the reorientation of polar side groups due to interaction with NPs, consequently restricting the macromolecular motions [23,33]. Also, the  $M''$  spectra of CPN revealed anomalous shift of

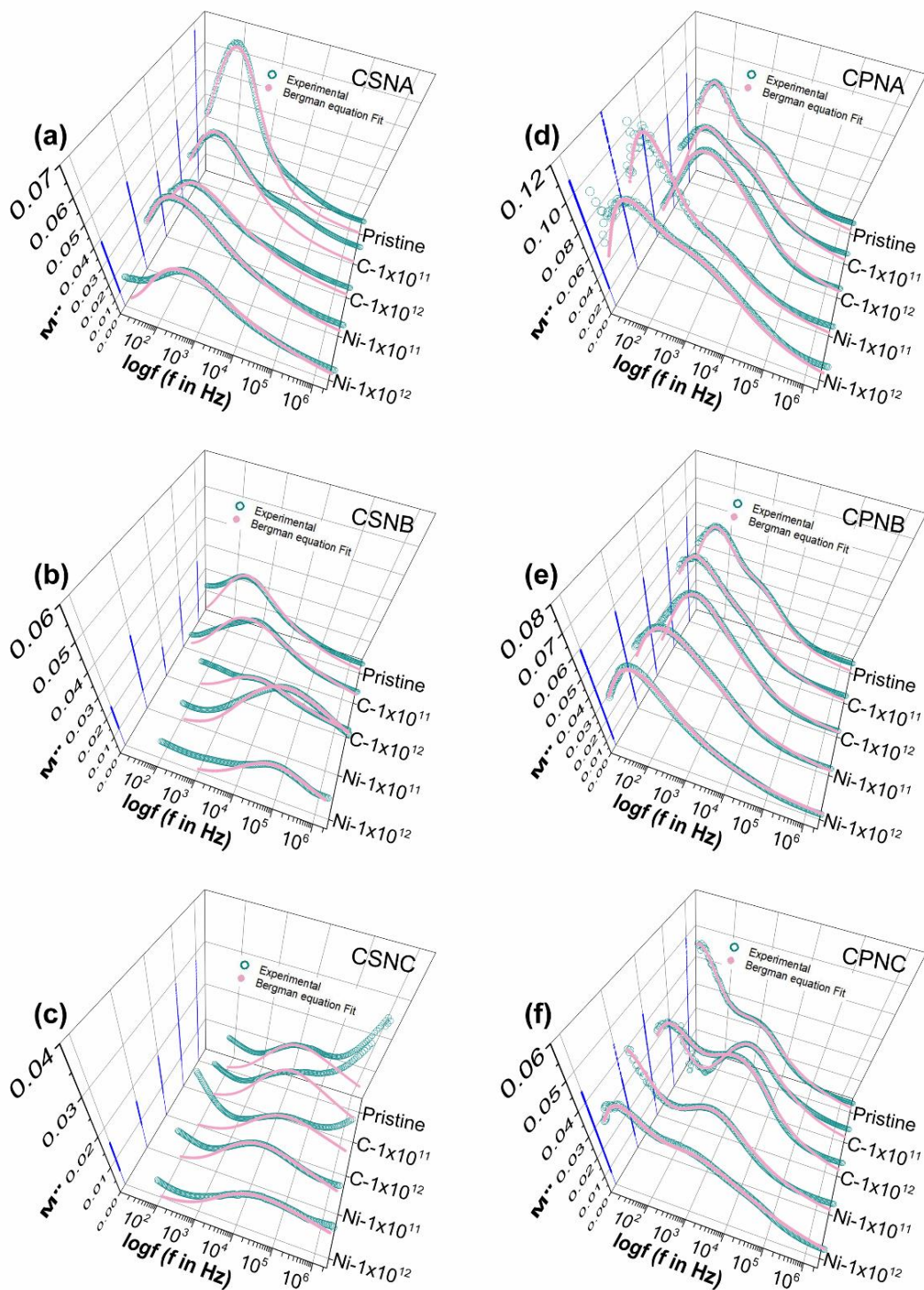


**Figure 5.15** Plot of imaginary part of electric modulus versus log frequency for (a) CSNA, (b) CSNB, (c) CSNC, (d) CPNA, (e) CPNB, and (f) CPNC matrices irradiated with  $C^{+5}$  and  $Ni^{+7}$  ions at the fluence of  $1 \times 10^{11}$  and  $1 \times 10^{12}$  ions/cm<sup>2</sup>, respectively.

**Table 5.3** Parameter values obtained from the Bergman equation fit of pristine and irradiated CSN matrices with 60-MeV C<sup>+5</sup> and 100-MeV Ni<sup>+7</sup> ions at the fluence of 1×10<sup>11</sup> and 1×10<sup>12</sup> ions/cm<sup>2</sup>.

Sample	$M''_{max}$	$f_{max}$	$\beta_{KWW}$	FOM (%)
CSNA	0.10100	217	0.52577	9.83
CSNA (C-1×10 <sup>11</sup> ions/cm <sup>2</sup> )	0.07078	250	0.41480	14.82
CSNA (C-1×10 <sup>12</sup> ions/cm <sup>2</sup> )	0.05778	265	0.35581	12.82
CSNA (Ni-1×10 <sup>11</sup> ions/cm <sup>2</sup> )	0.07557	350	0.32577	4.99
CSNA (Ni-1×10 <sup>12</sup> ions/cm <sup>2</sup> )	0.06241	1600	0.31524	8.73
CSNB	0.04488	770	0.39114	9.61
CSNB (C-1×10 <sup>11</sup> ions/cm <sup>2</sup> )	0.03951	2800	0.29542	7.00
CSNB (C-1×10 <sup>12</sup> ions/cm <sup>2</sup> )	0.02435	13000	0.34542	4.06
CSNB (Ni-1×10 <sup>11</sup> ions/cm <sup>2</sup> )	0.05816	13000	0.22114	9.88
CSNB (Ni-1×10 <sup>12</sup> ions/cm <sup>2</sup> )	0.03444	140000	0.39745	6.18
CSNC	0.02690	43870	0.24855	5.05
CSNC (C-1×10 <sup>11</sup> ions/cm <sup>2</sup> )	0.02680	44000	0.28847	10.30
CSNC (C-1×10 <sup>12</sup> ions/cm <sup>2</sup> )	0.02247	100547	0.24180	7.63
CSNC (Ni-1×10 <sup>11</sup> ions/cm <sup>2</sup> )	0.02617	45000	0.24642	1.73
CSNC (Ni-1×10 <sup>12</sup> ions/cm <sup>2</sup> )	0.02611	135000	0.20121	3.62

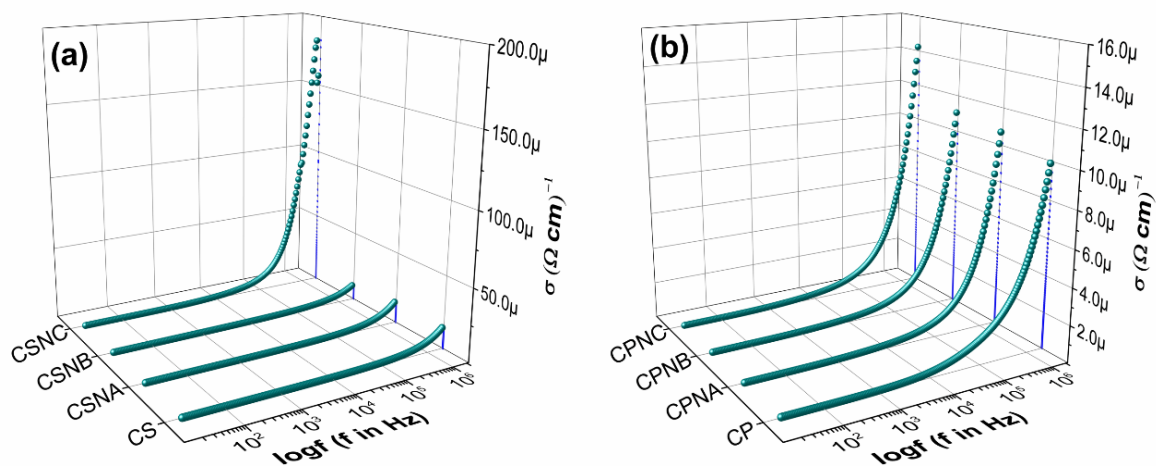
**Table 5.4** Parameter values obtained from the Bergman equation fit of pristine and irradiated CSN matrices with 60-MeV C<sup>+5</sup> and 100-MeV Ni<sup>+7</sup> ions at the fluence of 1×10<sup>11</sup> and 1×10<sup>12</sup> ions/cm<sup>2</sup>.

Sample	Peak at low frequency			Peak at high frequency			FOM (%)
	$M''_{max}$	$f_{max}$	$\beta_{KWW}$	$M''_{max}$	$f_{max}$	$\beta_{KWW}$	
CPNA	0.12154	80	0.78551	0.06875	3620	0.44555	5.86
CPNA (C-1×10 <sup>11</sup> ions/cm <sup>2</sup> )	0.10245	141	0.73935	0.06866	4200	0.42488	5.97
CPNA (C-1×10 <sup>12</sup> ions/cm <sup>2</sup> )	0.09985	270	0.58097	0.06981	4300	0.35562	4.14
CPNA (Ni-1×10 <sup>11</sup> ions/cm <sup>2</sup> )	0.16245	90	0.73214	0.06079	4450	0.42473	8.73
CSNA (Ni-1×10 <sup>12</sup> ions/cm <sup>2</sup> )	0.14651	160	0.62034	0.08976	8850	0.36411	6.13
CPNB	0.08185	100	0.64424	0.03475	3880	0.48314	6.96
CPNB (C-1×10 <sup>11</sup> ions/cm <sup>2</sup> )	0.08277	100	0.51352	0.02407	4250	0.41321	3.68
CPNB (C-1×10 <sup>12</sup> ions/cm <sup>2</sup> )	0.07777	280	0.48382	0.01621	4410	0.25304	5.39
CPNB (Ni-1×10 <sup>11</sup> ions/cm <sup>2</sup> )	0.08282	210	0.41587	0.01422	4410	0.26321	3.92
CPNB (Ni-1×10 <sup>12</sup> ions/cm <sup>2</sup> )	0.08112	190	0.45624	0.01315	9110	0.24980	4.69
CPNC	0.07085	36	0.64614	0.03275	3910	0.40482	3.04
CPNC (C-1×10 <sup>11</sup> ions/cm <sup>2</sup> )	0.04857	11	0.63652	0.04767	3520	0.42144	7.78
CPNC (C-1×10 <sup>12</sup> ions/cm <sup>2</sup> )	0.06055	70	0.61624	0.04915	5500	0.41985	3.13
CPNC (Ni-1×10 <sup>11</sup> ions/cm <sup>2</sup> )	0.06461	25	0.71618	0.04582	3520	0.41282	4.91
CPNC (Ni-1×10 <sup>12</sup> ions/cm <sup>2</sup> )	0.05957	80	0.63614	0.04215	9500	0.28985	2.85

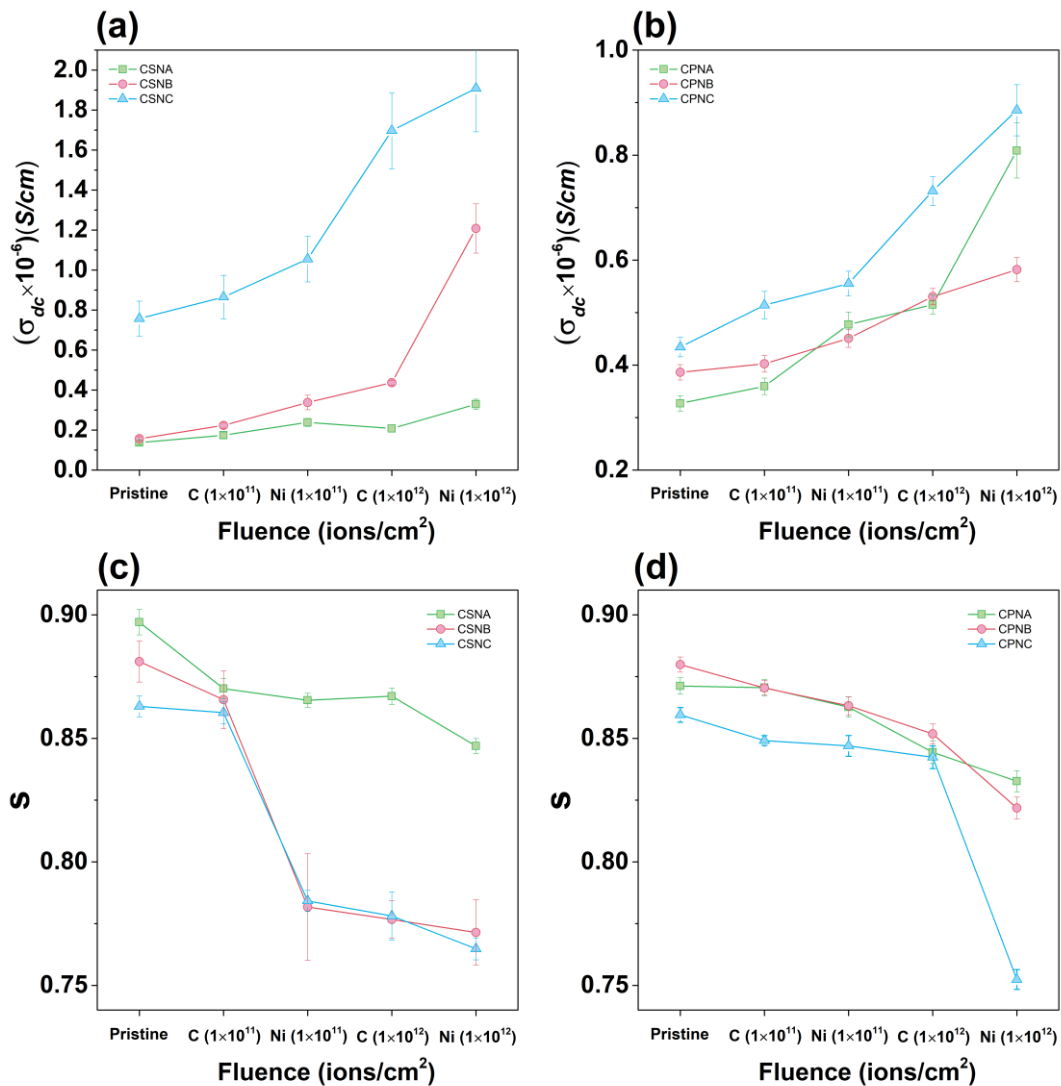
relaxation peak appeared at a lower frequency, whereas, the relaxation peak evolved at high frequency window is shifted to higher frequency. This deviation in the imaginary modulus profile indicates that the localized environment of CPN is modified upon filler loading.

The variation of imaginary part of electric modulus as a function of log frequency for pre and post  $C^{+5}$  and  $Ni^{+7}$  ions irradiated CSN, and CPN matrices at the fluence of  $1 \times 10^{11}$  and  $1 \times 10^{12}$  ions/cm<sup>2</sup> are illustrated in Figure 5.15. The graphics show a remarkable amendment in the relaxation phenomena of macromolecule with confinement of NPs is affected by beam parameters. The shifting in relaxation peak is due to the long drift of trapped charge carriers, released from the defect sites upon irradiation [7,19].

Each  $M''$  spectra is fitted using a fit-function developed by Bergman, as discussed in section 2.4.4 of Chapter 2. The double relaxation peaks are fitted using two Bergman functions [34]. Due to deviation in fitting at the high-frequency window, the good fitting is focused around the peak and monitor using the figure of merit (FOM) evaluation. The solid symbol in Figure 5.14 and Figure 5.15 is stands for the well-fitted modulus spectra as per the Bergman approach, whereas the hollow symbol depicts the experimental data. The parametric values of  $M''_{max}$ ,  $f_{max}$  and  $\beta_{KWW}$  are estimated from the fitting formalism for pre and post  $C^{+5}$  and  $Ni^{+7}$  ions irradiated CSN and CPN matrices at the fluence of  $1 \times 10^{11}$  and  $1 \times 10^{12}$  ions/cm<sup>2</sup> are summarised in Table 5.3 and Table 5.4, respectively. The shape parameter  $\beta_{KWW}$  for CSN matrices attained the values in the span of 0.53 to 0.20. For CPN, the  $\beta_{KWW}$  found between 0.83 to 0.42 and 0.45 to 0.25 for



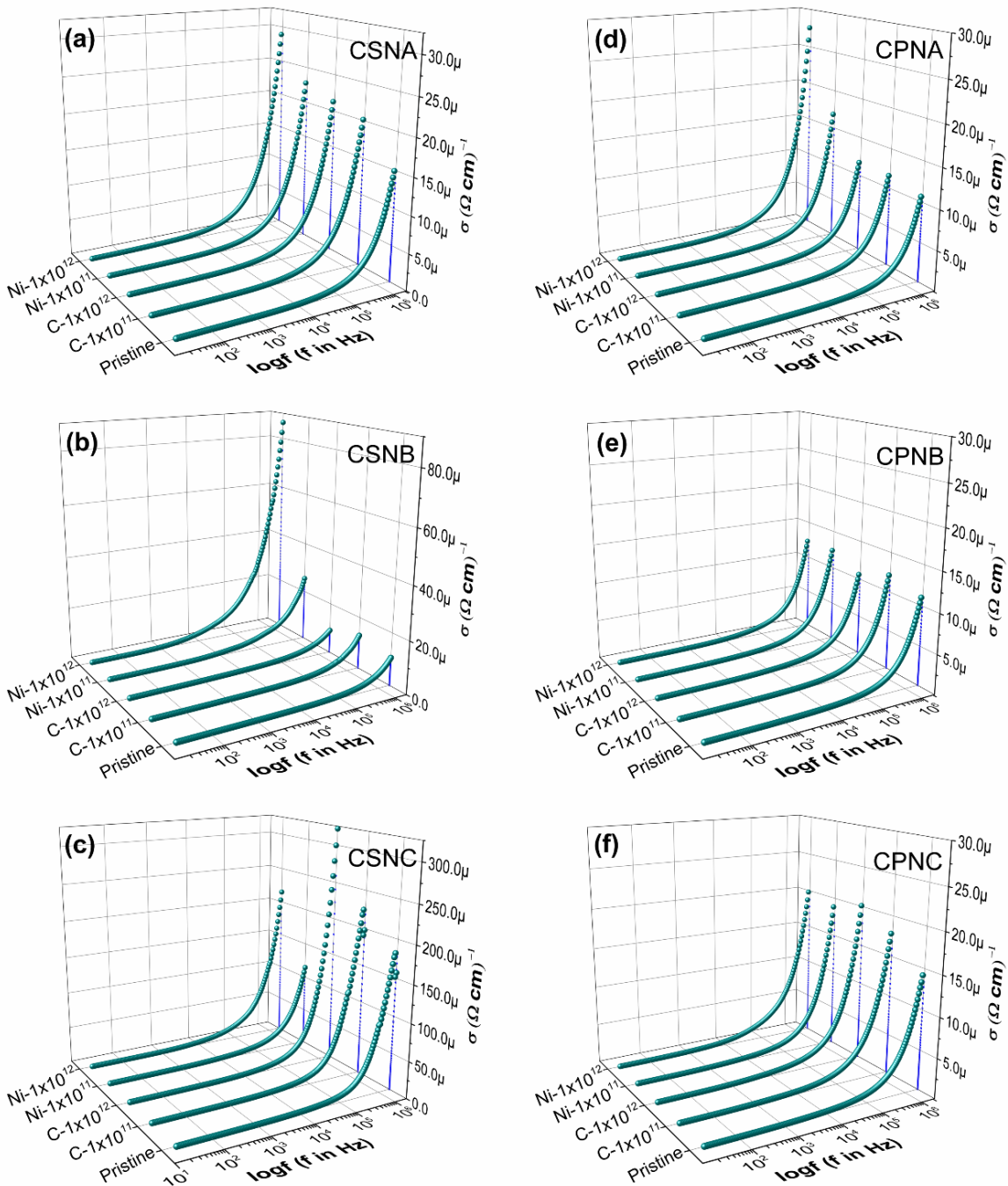
**Figure 5.16** Plot of conductivity versus log frequency of Ag NPs dependent (a) CSN and (b) CPN matrices, respectively.



**Figure 5.17** Variation in dc conductivity for (a) CSN and (b) CPN matrices as a function of ion fluence. Variation in frequency exponent “s” for (c) CSN and (d) CPN matrices as a function of ion fluence.

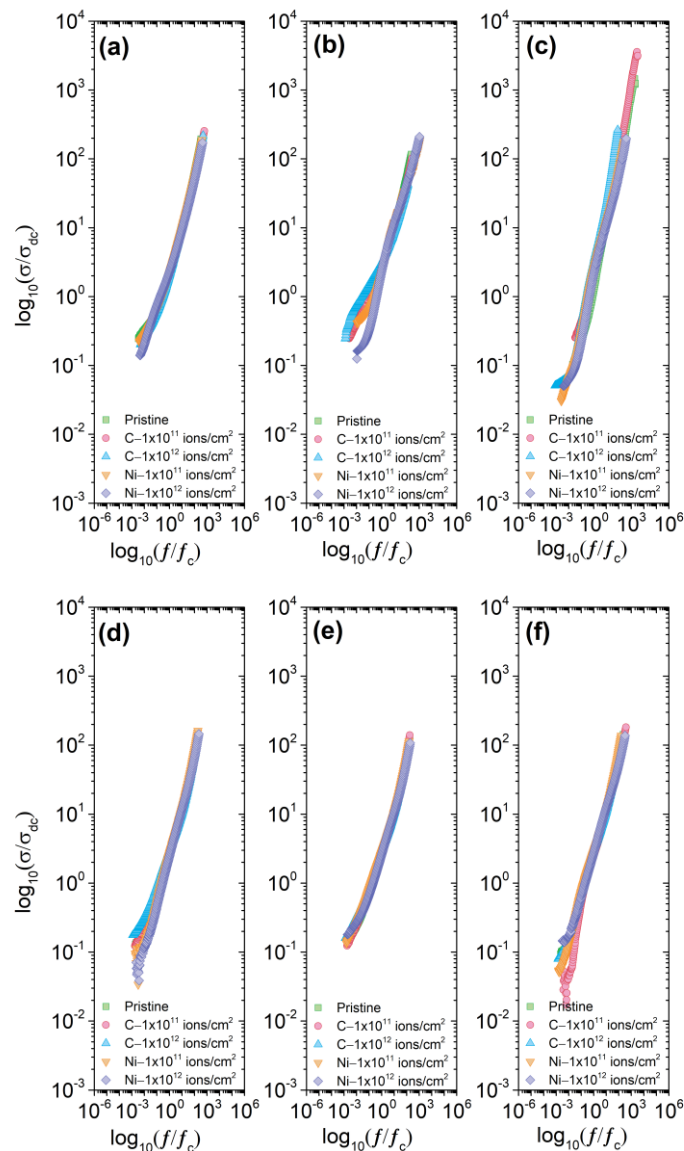
the relaxation peaks at low frequency and high frequency, respectively. Therefore, the relaxation events for both matrices are a non-Debye type. Also, the  $\beta_{KWW}$  values are relatively lower than unity, indicating that the relaxation event is non-exponential and charge carrier movement is cooperative events, that is, hopping from one site to adjacent site cannot be treated as an isolated event [35].

Figure 5.16 depicts the variation of total conductivity ( $\sigma$ ) as a function of log frequency for CSN and CPN matrices. Using the Jonscher universal power law [36], direct current,  $\sigma_{dc}$ , was



**Figure 5.18** Plot of conductivity versus log frequency for (a) CSNA, (b) CSNB, (c) CSNC, (d) CPNA, (e) CPNB, and (f) CPNC matrices irradiated with  $\text{C}^{+5}$  and  $\text{Ni}^{+7}$  ions at the fluence of  $1 \times 10^{11}$  and  $1 \times 10^{12}$  ions/cm<sup>2</sup>, respectively.

estimated by extrapolating of the plateau region of  $\sigma$  to zero frequency. As observed from Figure 5.17 that the  $\sigma_{\text{dc}}$  raise moderately upon increasing the Ag NPs composition for both matrices. A similar trend is also perceived for Ag NPs based polymer nanocomposites systems



**Figure 5.19** Scaling of the conductivity spectra for (a) CSNA, (b) CSNB, (c) CSNC, (d) CPNA, (e) CPNB and (f) CPNC matrices irradiated with  $C^{+5}$  and  $Ni^{+7}$  ions at the fluence of  $1 \times 10^{11}$  and  $1 \times 10^{12}$  ions/cm<sup>2</sup>, respectively.

[5,9,26,27]. This is assigned to the crystalline phase of PEO in CPN matrices, responsible for the impeded hopping processes between coordination sites.

Figure 5.18 presents the variation of frequency-dependent total conductivity for pre and post  $C^{+5}$  and  $Ni^{+7}$  ions irradiated CSN and CPN matrices. It is noted that higher fluence and  $Ni^{+7}$  ions enhances the conductivity more effectively. Ion with superior  $S_e$  value may profoundly establish the carbonaceous clustering, enhancing the correlation length facilitating cluster-to-cluster communications [19,21,25–27]. Also, the rise in frequency-dependent ac conductivity,  $\sigma_{ac}$ , at high frequency window is perceived upon irradiation. It is attributed to enhanced charge

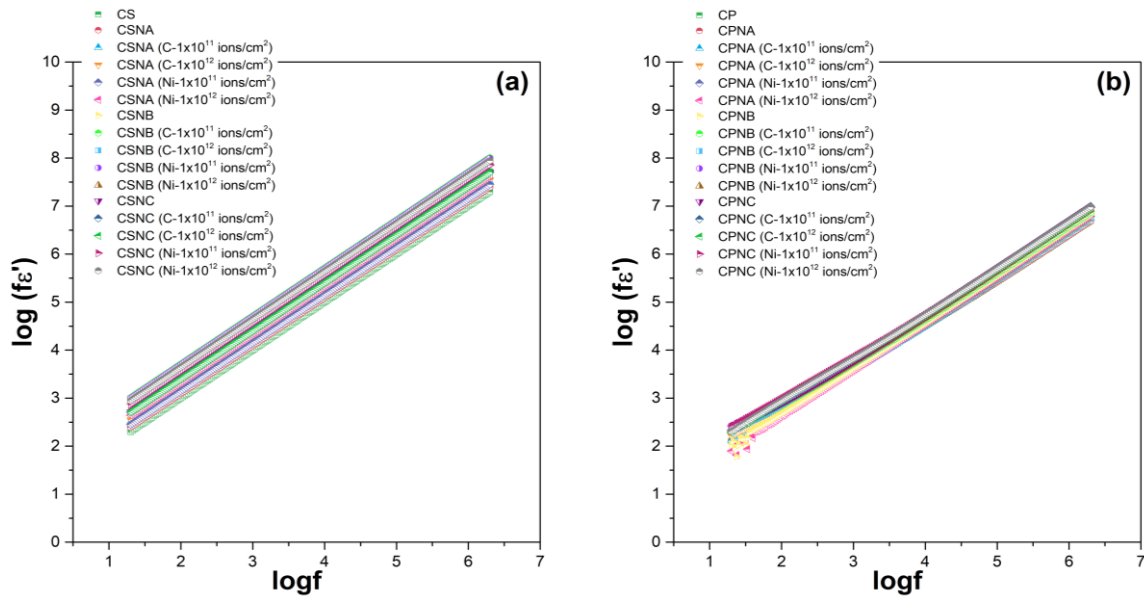


**Figure 5.20** Plot of  $\log(fe')$  versus  $\log$  frequency of (a) CSN and (b) CPN matrices irradiated with  $C^{+5}$  and  $Ni^{+7}$  ions at the fluence of  $1 \times 10^{11}$  and  $1 \times 10^{12}$  ions/cm<sup>2</sup>, respectively.

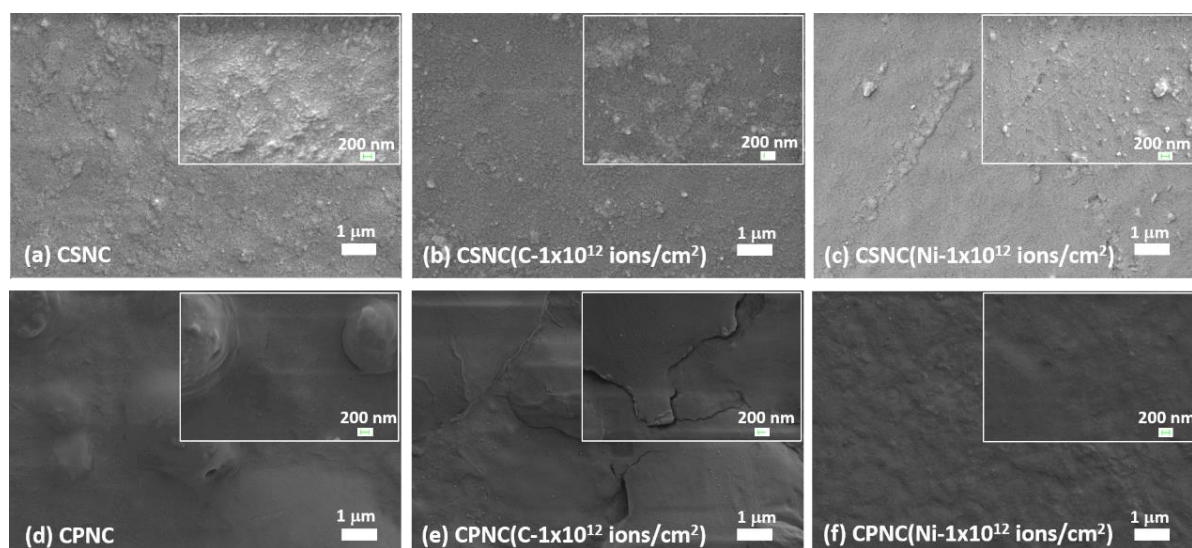
carriers density, chain scission and formation of C=O, C=C and C=NH linkages. The flexible materials with high dielectric constant and conductivity are highly important and can be utilized as electromagnetic interference shielding materials.

To comprehend the dependence of conductivity relaxation dynamics on the MeV ions irradiation, the conductivity spectra's scaling has been investigated. Figure 5.19 represents the scaling plots of total conductivity of pre and post  $C^{+5}$  and  $Ni^{+7}$  ions irradiated CSN and CPN matrices at different ion fluences. The scaling procedure is performed as per the literature reported elsewhere [35,37]. It is observed that the spectra of each sample irradiated with carbon and nickel ions at different fluences merge to a single master curve. The spectra's superior overlapping implies that conductivity relaxation in the nanocomposites matrices is independent of beam parameters.

The frequency exponent “s” calculated as per the formalism described in section 2.4.4 of Chapter 2. The variation of “s” with Ag NPs composition and beam parameters for CSN and CPN is shown in Figure 5.17(c) and Figure 5.17(d), respectively. The values of “s” is decreased with increasing fluence. It is found that the values are varied between 0.90 to 0.76 for CSN and 0.87 to 0.75 for CPN matrices. This indicates hopping of charge carriers is a suitable conduction mechanism, and it is AC type [36].

Kramer-Krönig interpretation presents an appropriate perceptive of the variation of power-law exponent. In this approach,  $\epsilon'$  is proportional to  $f^{m-1}$ , which can be expressed as  $\epsilon'f = Bf^m$ , where  $m$  is the exponent [38]. Therefore,  $\log(f\epsilon') \rightarrow \log f$  plot over a broad spectrum of frequency range has a linear response with a slope of  $m$  [38]. This kind of trend is observed in Figure 5.20 for CSN and CPN matrices. This is credited to the universal dielectric response (UDR) model's well-defined dominance. The hopping of charge carriers between adjacent sites coupled with the dipolar relaxation, generally, observed in a persuasive disordered/amorphous materials [39,40].

### 5.2.5 SEM Analysis



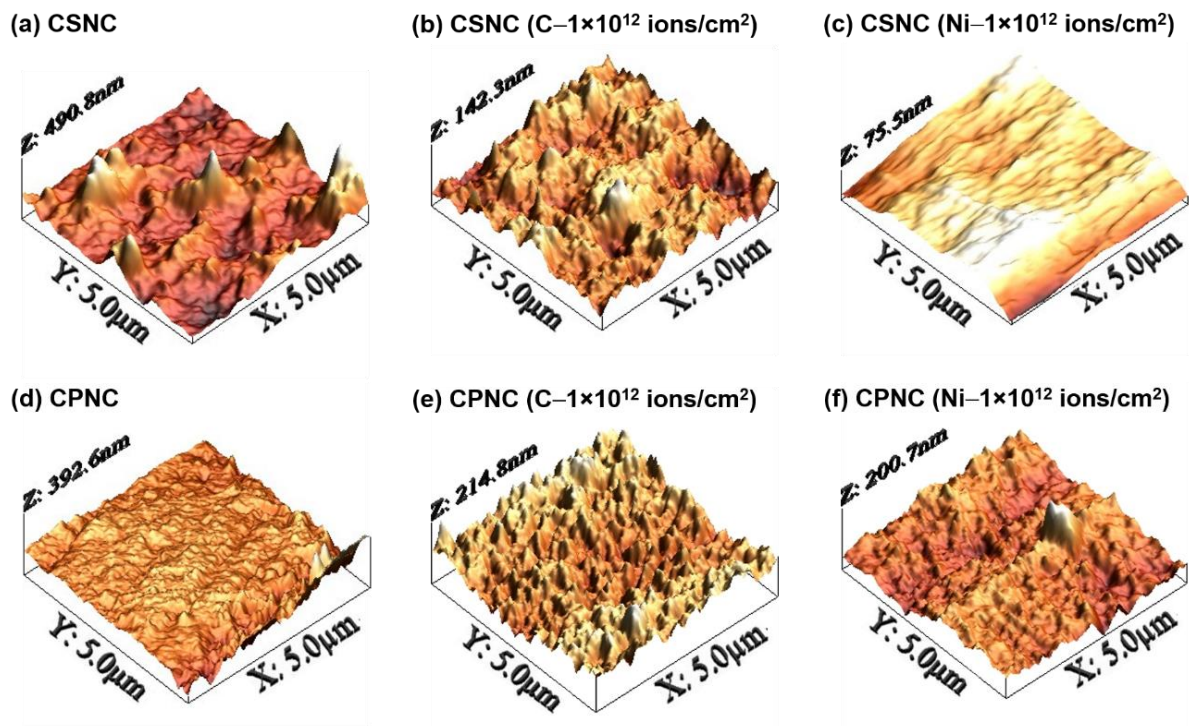
**Figure 5.21** FESEM micrographs of (a) CSNC irradiated with (b)  $C^{+5}$  ions, (c)  $Ni^{+7}$  ions at the fluence of  $1 \times 10^{12}$  ions/cm<sup>2</sup> and (d) CPNC irradiated with (e)  $C^{+5}$  ions (f)  $Ni^{+7}$  ions at the fluence of  $1 \times 10^{12}$  ions/cm<sup>2</sup>.

Figure 5.21(a–f) depicts the FESEM micrographs of  $C^{+5}$  and  $Ni^{+7}$  ions irradiated CSNC (Figure 5.21(a–c)) and CPNC (Figure 5.21(d–f)) matrices at a fluence of  $1 \times 10^{12}$  ions/cm<sup>2</sup>. The SEM images present with 1  $\mu$ m and 200 nm scales at 25 K $\times$  and 50 K $\times$  magnifications, respectively. The FESEM image of CSNC (Figure 5.21(a)) reveals a non-porous and crack-free surface with some species of NPs. Whereas, the CPNC (Figure 5.21(d)) shows dissimilar sized nodules indicating the presence of spherulites crystalline structure of PEO. Both matrices exhibit porous free morphology is ascribed to better surface packing owing to electrostatic interaction between polymeric chains and Ag NPs, mainly at the interphase. Also, the silver nanoparticle might aptly be distributed in matrices. Upon  $C^{+5}$  ions irradiation, the surface of CSNC (Figure

5.21(b)) becomes smooth with some specs, whereas, little phase separation is perceived for CPNC (Figure 5.21(e)). For the case of  $\text{Ni}^{+7}$  ions irradiation, the surface morphology becomes considerably smoother for both the matrices (Figure 5.21(c and f)), which directly belong to the amorphous phase of the polymer nanocomposites. The XRD results are closely associated with the FESEM micrographs. The irradiation promotes the temperature within the picosecond time nearby the ion trajectory [41]. Afterward, the polymeric chains rearrange themselves and yielded enhanced interfacial interaction with NPs in association with new chemical linkages and defects [21,25,42]. The rapid quenching phenomenon is rising with increasing ion fluence. Then, there is an overlapping of ion trajectories, consequently, yielded a carbon-rich network with an enhanced conjugated system.

## 5.2.6 AFM Analysis

Figure 5.22(a–f) demonstrate illustrative AFM micrographs of  $\text{C}^{+5}$  and  $\text{Ni}^{+7}$  ions irradiated CSNC (Figure 5.22(a–c)) and CPNC (Figure 5.22(d–f)) matrices at a fluence of  $1 \times 10^{12}$  ions/cm<sup>2</sup>. The AFM images of CSNC (Figure 5.22(a)) have sharp hillock-like structures. While CPNC (Figure 5.22(b)) exhibits, homogeneous, and smoother morphology is attributed to the



**Figure 5.22** AFM images of (a) CSNC irradiated with (b)  $\text{C}^{+5}$  ions, (c)  $\text{Ni}^{+7}$  ions at the fluence of  $1 \times 10^{12}$  ions/cm<sup>2</sup> and (d) CPNC irradiated with (e)  $\text{C}^{+5}$  ions (f)  $\text{Ni}^{+7}$  ions at the fluence of  $1 \times 10^{12}$  ions/cm<sup>2</sup>.

compatibilizing effect of Ag NPs [43]. The parametric values, namely, Root Mean Square (RMS) roughness ( $R_q$ ) and average roughness ( $R_a$ ), are evaluated for the morphological studies. The obtained values of  $R_q$  and  $R_a$  for CSNC are 71.2 nm and 50.3 nm, respectively. Whereas, for CPNC, the corresponding values are 33.6 nm and 23.5 nm, respectively. Relatively rough morphology of CSNC is promoted by espies of metal NPs over the surfaces. For  $C^{+5}$  and  $Ni^{+7}$  ions irradiated CSNC sample, the value of  $R_q$  diminished to 19.2 nm and 12.3 nm, whereas the value of  $R_a$  reduced to 15.2 nm and 9.4 nm, respectively. For  $C^{+5}$  and  $Ni^{+7}$  ions irradiated CPNC sample, the value of  $R_q$  moderated to 21.4 nm and 20.4 nm, whereas the value of  $R_a$  lowered to 15.7 nm and 16.2 nm, respectively. The decrease in surface parametric values due to irradiation indicates significantly smoother morphology. These verdicts indorsed to the imperative collision level of massive ions on the surface of relatively soft materials might wreck the hill-like topographies and caused localized surface diffusion of NPs within the matrix. The AFM study is found to be in accordance with the SEM imaging involving the qualitatively and quantitatively evaluations of the polymer nanocomposites' morphological features.

### 5.3 Conclusions

The self-sustained nanocomposites matrices of chitosan and (chitosan-PEO) with 5, 10 and 15 wt% of silver nanoparticles were prepared *via* solution casting approach. These matrices were irradiated under high vacuum conditions with carbon and nickel ions of energy 60 MeV and 100 MeV at fluence of  $1 \times 10^{11}$  and  $1 \times 10^{12}$  ions/cm<sup>2</sup>, respectively. XRD studies revealed amendments in polymer-nanoparticle and polymer-polymer interaction with composition level. These matrices exhibit a dominant amorphous phase; however, the existence of the spherulites structure of PEO ensures the crystalline phase. The crystallite size shows an increasing trend with composition; on another hand, it decreases with increasing fluence. An overall amorphization of the nanocomposites system due to MeV ions irradiation is also noticed from the XRD analysis. ATR-FTIR analysis showed that the inclusion of NPs moderates the interaction among main and side-chain functional groups. The shift of vibration modes to the lower wavenumber with broadening and merging with increasing additive level is also perceived due to the interaction between functional groups of polymer and nanoparticles. The degradation of macromolecular due to the rupture of numerous polymeric linkages owing to SHIs irradiation. The carbonyl band evolved as a result of ions polymer interactions for CSN

matrices, while CPN matrices confirmed the mutual stabilizing effect. The matrices irradiated with  $1 \times 10^{12}$  ions/cm<sup>2</sup> have substantially high absorbance across the UV regime and have comparatively lower absorption in the visible region. Which confirms their suitable relevance as UV shielding and optical filters. Moreover, the bandgap can reliably tailored by varying the beam parameters of both matrices, which comprehend the materials as bandgap tuner in optical devices. The frequency-dependent dielectric constant and conductivity enhance with composition and fluence recognize their relevance as electromagnetic interference shielding. These materials follow the universal dielectric response. The SEM analysis supports the XRD data. AFM studies showed that surface morphology becomes smoother upon MeV ions irradiation.

## REFERENCES

- [1] K.K. Sadasivuni, D. Ponnamma, J. Kim, J.J. Cabibihan, M.A. AlMaadeed, *Biopolymer Composites in Electronics*, Elsevier, 2017. doi:10.1016/C2014-0-04575-3.
- [2] W.J. Parak, L. Manna, F.C. Simmel, D. Gerion, P. Alivisatos, *Nanoparticles: From Theory to Application, Ch2; Quantum Dots*, 2004. doi:10.1002/3527602399.ch2.
- [3] D. Moura, J.F. Mano, M.C. Paiva, N.M. Alves, Chitosan nanocomposites based on distinct inorganic fillers for biomedical applications, *Sci. Technol. Adv. Mater.* 17 (2016) 626–643. doi:10.1080/14686996.2016.1229104.
- [4] B. Wang, W. Huang, L. Chi, M. Al-Hashimi, T.J. Marks, A. Facchetti, High- $k$  Gate Dielectrics for Emerging Flexible and Stretchable Electronics, *Chem. Rev.* 118 (2018) 5690–5754. doi:10.1021/acs.chemrev.8b00045.
- [5] S. Kumar-Krishnan, E. Prokhorov, M. Hernández-Iturriaga, J.D. Mota-Morales, M. Vázquez-Lepe, Y. Kovalenko, I.C. Sanchez, G. Luna-Bárceñas, Chitosan/silver nanocomposites: Synergistic antibacterial action of silver nanoparticles and silver ions, *Eur. Polym. J.* 67 (2015) 242–251. doi:10.1016/j.eurpolymj.2015.03.066.
- [6] A.L. Patterson, The Scherrer Formula for X-Ray Particle Size Determination, *Phys. Rev.* 56 (1939) 978–982. doi:10.1103/PhysRev.56.978.
- [7] V. Kumar, *Radiation Effects in Polymeric Materials*, Springer International Publishing, Cham, 2019. doi:10.1007/978-3-030-05770-1.
- [8] D. Wei, W. Qian, Facile synthesis of Ag and Au nanoparticles utilizing chitosan as a mediator agent, *Colloids Surfaces B Biointerfaces.* 62 (2008) 136–142. doi:10.1016/j.colsurfb.2007.09.030.
- [9] J.B. González-Campos, J.D. Mota-Morales, S. Kumar, D. Zárte-Triviño, M. Hernández-Iturriaga, Y. Prokhorov, M.V. Lepe, Z.Y. García-Carvajal, I.C. Sanchez, G. Luna-Bárceñas, New insights into the bactericidal activity of chitosan-Ag bionanocomposite: The role of the electrical conductivity, *Colloids Surfaces B Biointerfaces.* 111 (2013) 741–746. doi:10.1016/j.colsurfb.2013.07.003.
- [10] J. Kowalonek, Surface and thermal behavior of chitosan/poly(ethylene oxide) blends, *Mol. Cryst. Liq. Cryst.* 640 (2016) 78–89. doi:10.1080/15421406.2016.1255518.
- [11] G.B. Patel, S. Bhavsar, N.L. Singh, F. Singh, P.K. Kulriya, SHI induced modification in structural, optical, dielectric and thermal properties of poly ethylene oxide films, *Nucl. Instruments Methods Phys. Res. Sect. B Beam Interact. with Mater. Atoms.* 379 (2016) 156–161. doi:10.1016/j.nimb.2016.04.018.
- [12] S. Bonardd, M. Schmidt, M. Saavedra-Torres, A. Leiva, D. Radic, C. Saldías, Thermal and morphological behavior of chitosan/PEO blends containing gold nanoparticles. Experimental and theoretical studies, *Carbohydr. Polym.* 144 (2016) 315–329. doi:10.1016/j.carbpol.2016.02.071.

- [13] H. Mortazavian, C.J. Fennell, F.D. Blum, Structure of the Interfacial Region in Adsorbed Poly(vinyl acetate) on Silica, *Macromolecules*. 49 (2016) 298–307. doi:10.1021/acs.macromol.5b02214.
- [14] N. Karak, Fundamentals of Nanomaterials and Polymer Nanocomposites, in: *Nanomater. Polym. Nanocomposites*, Elsevier, 2019: pp. 1–45. doi:10.1016/B978-0-12-814615-6.00001-1.
- [15] N. Punitha, P.S. Ramesh, D. Geetha, Spectral, morphological and antibacterial studies of  $\alpha$ -cyclodextrin stabilized silver - Chitosan nanocomposites, *Spectrochim. Acta - Part A Mol. Biomol. Spectrosc.* 136 (2015) 1710–1717. doi:10.1016/j.saa.2014.10.071.
- [16] B.N.J. Persson, Polarizability of small spherical metal particles: influence of the matrix environment, *Surf. Sci.* 281 (1993) 153–162. doi:10.1016/0039-6028(93)90865-H.
- [17] M.A. Garcia, Surface plasmons in metallic nanoparticles: fundamentals and applications, *J. Phys. D. Appl. Phys.* 44 (2011) 283001. doi:10.1088/0022-3727/44/28/283001.
- [18] E. Zojer, T.C. Taucher, O.T. Hofmann, The Impact of Dipolar Layers on the Electronic Properties of Organic/Inorganic Hybrid Interfaces, *Adv. Mater. Interfaces*. 6 (2019) 1900581. doi:10.1002/admi.201900581.
- [19] D. Fink, Fundamentals of Ion-Irradiated Polymers, Springer Berlin Heidelberg, Berlin, Heidelberg, 2004. doi:10.1007/978-3-662-07326-1.
- [20] Y.K. Mishra, S. Mohapatra, V.S.K. Chakravadhanula, N.P. Lalla, V. Zaporozhchenko, D.K. Avasthi, F. Faupel, Synthesis and Characterization of Ag-Polymer Nanocomposites, *J. Nanosci. Nanotechnol.* 10 (2010) 2833–2837. doi:10.1166/jnn.2010.1449.
- [21] G. Compagnini, G. Foti, R. Reitano, G. Mondio, Graphitic clusters in hydrogenated amorphous carbon induced by keV-ion irradiation, *Appl. Phys. Lett.* 57 (1990) 2546–2548. doi:10.1063/1.103832.
- [22] C. Hendrich, J. Bosbach, F. Stietz, F. Hubenthal, T. Vartanyan, F. Träger, Chemical interface damping of surface plasmon excitation in metal nanoparticles: a study by persistent spectral hole burning, *Appl. Phys. B*. 76 (2003) 869–875. doi:10.1007/s00340-003-1168-9.
- [23] G.C. Psarras, Conductivity and dielectric characterization of polymer nanocomposites, in: *Phys. Prop. Appl. Polym. Nanocomposites*, Elsevier, 2010: pp. 31–69. doi:10.1533/9780857090249.1.31.
- [24] F. Kremer, A. Schönhals, Broadband Dielectric Spectroscopy, Springer Berlin Heidelberg, Berlin, Heidelberg, 2003. doi:10.1007/978-3-642-56120-7.
- [25] A. Biswas, D.K. Avasthi, D. Fink, J. Kanzow, U. Schürmann, S.J. Ding, O.C. Aktas, U. Saeed, V. Zaporozhchenko, F. Faupel, R. Gupta, N. Kumar, Nanoparticle architecture in carbonaceous matrix upon swift heavy ion irradiation of polymer-metal

- nanocomposites, *Nucl. Instruments Methods Phys. Res. Sect. B Beam Interact. with Mater. Atoms.* 217 (2004) 39–50. doi:10.1016/j.nimb.2003.09.032.
- [26] C. Gavade, N.L. Singh, A. Sharma, P.K. Khanna, F. Singh, The effect of SHI irradiation on structural, thermal and dielectric properties of a silver nanoparticle-embedded polystyrene matrix, *Radiat. Eff. Defects Solids.* 166 (2011) 585–591. doi:10.1080/10420150.2011.579123.
- [27] C. Gavade, N.L. Singh, P.K. Khanna, Optical and Dielectric Properties of Ion Beam Irradiated Ag/Polymethyl Methacrylate Nanocomposites, *J. Nanosci. Nanotechnol.* 14 (2014) 5911–5916. doi:10.1166/jnn.2014.8736.
- [28] C.C. Ku, R. Liepins, *Electrical properties of polymers*, Hanser Publishers New York, 1987.
- [29] G. Williams, D.C. Watts, Non-symmetrical dielectric relaxation behaviour arising from a simple empirical decay function, *Trans. Faraday Soc.* 66 (1970) 80. doi:10.1039/tf9706600080.
- [30] R. Bergman, General susceptibility functions for relaxations in disordered systems, *J. Appl. Phys.* 88 (2000) 1356–1365. doi:10.1063/1.373824.
- [31] S.B. Aziz, Z.H. Z. Abidin, A. K. Arof, Influence of silver ion reduction on electrical modulus parameters of solid polymer electrolyte based on chitosan-silver triflate electrolyte membrane, *Express Polym. Lett.* 4 (2010) 300–310. doi:10.3144/expresspolymlett.2010.38.
- [32] G.B. Patel, N.L. Singh, F. Singh, Modification of chitosan-based biodegradable polymer by irradiation with MeV ions for electrolyte applications, *Mater. Sci. Eng. B.* 225 (2017) 150–159. doi:10.1016/j.mseb.2017.08.023.
- [33] G.A. Kontos, A.L. Soulintzis, P.K. Karahaliou, G.C. Psarras, S.N. Georga, C.A. Krontiras, M.N. Pisanias, Electrical relaxation dynamics in TiO<sub>2</sub> – polymer matrix composites, *Express Polym. Lett.* 1 (2007) 781–789. doi:10.3144/expresspolymlett.2007.108.
- [34] S. Kamoun, M. Gargouri, Electrical conductivity and complex electric modulus of NaCuFe<sub>2</sub>(VO<sub>4</sub>)<sub>3</sub> material, *Ionics (Kiel)*. 21 (2015) 765–774. doi:10.1007/s11581-014-1228-7.
- [35] A. Karmakar, A. Ghosh, Charge carrier dynamics and relaxation in (polyethylene oxide-lithium-salt)-based polymer electrolyte containing 1-butyl-1-methylpyrrolidinium bis(trifluoromethylsulfonyl)imide as ionic liquid, *Phys. Rev. E.* 84 (2011) 051802. doi:10.1103/PhysRevE.84.051802.
- [36] A.K. Jonscher, *Universal relaxation law: a sequel to Dielectric relaxation in solids*, Chelsea Dielectrics Press, 1996.
- [37] A. Ghosh, A. Pan, Scaling of the conductivity spectra in ionic glasses: Dependence on the structure, *Phys. Rev. Lett.* 84 (2000) 2188–2190. doi:10.1103/PhysRevLett.84.2188.

- [38] S. Ke, H. Huang, L. Ren, Y. Wang, Nearly constant dielectric loss behavior in poly(3-hydroxybutyrate- co -3-hydroxyvalerate) biodegradable polyester, *J. Appl. Phys.* 105 (2009) 096103. doi:10.1063/1.3125271.
- [39] S. Elliott, Frequency-dependent conductivity in ionically and electronically conducting amorphous solids, *Solid State Ionics.* 70–71 (1994) 27–40. doi:10.1016/0167-2738(94)90284-4.
- [40] C.R. Bowen, D.P. Almond, Modelling the “universal” dielectric response in heterogeneous materials using microstructural electrical networks, *Mater. Sci. Technol.* 22 (2006) 719–724. doi:10.1179/174328406X101328.
- [41] D.K. Avasthi, G.K. Mehta, *Swift Heavy Ions for Materials Engineering and Nanostructuring*, Springer Netherlands, Dordrecht, 2011. doi:10.1007/978-94-007-1229-4.
- [42] N.L. Singh, A. Qureshi, F. Singh, D.K. Avasthi, Effect of swift heavy ion irradiation on dielectrics properties of polymer composite films, *Mater. Sci. Eng. B.* 137 (2007) 85–92. doi:10.1016/j.mseb.2006.10.013.
- [43] S. Bonardd, M. Schmidt, M. Saavedra-Torres, A. Leiva, D. Radic, C. Saldías, Thermal and morphological behavior of chitosan/PEO blends containing gold nanoparticles. Experimental and theoretical studies, *Carbohydr. Polym.* 144 (2016) 315–329. doi:10.1016/j.carbpol.2016.02.071.